PF# 04-0078A

Study of long-time dynamics of a viscous vortex sheet with a fully adaptive non-stiff method

Hector D. Ceniceros

Department of Mathematics, University of California, Santa Barbara California 93106.[*]

Alexandre M. Roma

Department of Applied Mathematics,

University of Sao Paulo, Caixa Postal 66281,

CEP 05311-970, Sao Paulo-SP, Brazil.[†]

(Dated: June 18, 2004)

Abstract

A numerical investigation of the long-time dynamics of two immiscible two-dimensional fluids shearing past one another is presented. The fluids are incompressible and the interface between the bulk phases is subjected to surface tension. The simple case of density and viscosity matched fluids is considered. The two-dimensional Navier-Stokes equations are solved numerically with a novel fully adaptive *non-stiff* strategy based on the immersed boundary method. Dynamically adaptive mesh refinements are used to cover at all times the separately tracked fluid interface at the finest grid level. In addition, by combining adaptive front tracking, in the form of continuous interface marker equi-distribution, with a predictor-corrector discretization an efficient method is introduced to successfully treat the well-known numerical difficulties associated with surface tension. The resulting numerical method can be used to compute stably and with high resolution the flow for wide-ranging Weber numbers but this study focuses on the computationally challenging cases for which elongated fingering and interface roll-up are observed. To assess the importance of the viscous and vortical effects in the interfacial dynamics the full viscous flow simulations are compared with inviscid counterparts computed with a state-of-the-art boundary integral method. In the examined cases of roll-up, it is found that in contrast to the inviscid flow in which the interface undergoes a topological reconfiguration, the viscous interface remarkably escapes self-intersection and rich long-time dynamics due to separation, transport, and diffusion of vorticity is observed. An even more striking motion occurs at an intermediate Weber number for which elongated interpenetrating fingers of fluid develop. In this case, it is found that the Kelvin-Helmholtz instability weakens due to shedding of vorticity and unlike the inviscid counterpart in which there is indefinite finger growth the viscous interface is pulled back by surface tension. As the interface recedes, thin necks connecting pockets of fluid with the rest of the fingers form. Narrow jets are observed at the necking regions but the vorticity there ultimately appears to be insufficient to drain all the fluid and cause reconnection. However, at another point, two disparate portions of the interface come in close proximity as the interface continues to contract. Large curvature points and an intense concentration of vorticity are observed in this region and then the motion is abruptly terminated by the collapse of the interface.

PACS numbers: PACS 68.10.-m, 83.50.L, 63.10.Cr, 83.10.Lk

Keywords: Kelvin-Helmholtz instability; topological singularity; immersed boundary method; adaptive mesh refinements; adaptive front-tracking; vortex sheet roll-up; Navier-Stokes equations.

I. INTRODUCTION

When two immiscible fluids shear past one another they become the source of the Kelvin-Helmholtz (K-H) instability, one of the most fundamental instabilities in incompressible fluids. The free interface separating the two shearing fluids evolves dynamically driven by the K-H instability and competing regularizing effects such as surface tension and viscosity. The study of such a motion is of both fundamental and practical interest. Mixing in the ocean and the atmosphere as well as in engineering fluids such fuels and emulsions, are believed to be induced by instabilities of the K-H type and often these instabilities lead to turbulence[1].

The simplest model to study the K-H instability consists of two inviscid, immiscible, and irrotational density-matched fluids separated by a sharp fluid interface across which there is a discontinuity in tangential velocity. Because the flow vorticity is solely supported at the fluid interface this model is called a *vortex sheet*. Significant understanding of the K-H instability dynamics for *inviscid* flows has been obtained within this model. For example, in the absence of surface tension, it is known that the vortex sheet develops square-root isolated singularities in its curvature, well before roll-up can occur. The first analytic evidence of this was provided by Moore[2] by using asymptotic analysis near equilibrium. Subsequently, Caflisch and Orellana[3] extended Moore's analysis and found exact solutions to the approximate Moore's equations with finite-time singularity development. Numerically, evidence of the Moore's singularity has been provided by Krasny[4], Meiron, Baker, and Orszag[5], and Shelley[6] for a planar vortex sheet, and by Nie and Baker[7], Nitsche[8], and Sakajo[9] for the axi-symmetric geometry. Cowley, Baker, and Tanveer[10] demonstrated that Moore's singularities are quite generic for two-dimensional vortex sheets and more recently Hou, Hu, and Zhang[11] found that the same type of singularity is also present in a simplified model of a three-dimensional sheet.

The presence of surface tension leads to a rich variety of flow behavior as the study of Hou, Lowengrub, and Shelley[12], henceforth HLS, demonstrated for an inviscid vortex sheet. Particularly surprising dynamics occur for large and intermediate Weber numbers. The Weber number We provides a measure of the strength of the K-H instability relative to the dispersive regularization of surface tension. For intermediate We, the boundary integral simulations in Ref. 12 show the formation of elongating and inter-penetrating fingers of fluid.

At much larger We, where there are many unstable scales, the numerical study of HLS[12] reveals that the fluid interface rolls up into a spiral and its motion is later terminated by self-intersection of the fluid interface forming trapped fluid droplets. Thus, while regularizing Moore's singularity, surface tension leads yet to another type of singularity formation, a large-scale topological one. Even though pinching singularities are common in 3D and axi-symmetric free surface flows (e.g. jets) the formation of these types of singularities in 2D flows is less common and somewhat surprising. This is because the 2D flows lack the azimuthal surface tension force that is believed to play a crucial role in 3D fluid interface break-up.

It is natural to ask how small but finite viscosity would affect the surface tension mediated K-H dynamics. In a recent numerical study Tauber, Unverdi, and Tryggvason[13] show that, just as in the case of the inviscid vortex sheet, elongating fingers can develop in a sheared viscous interface for intermediate We. The simulations in Ref. 13 also show that there is separation and generation of a considerable amount of small-scale vorticity and increased interface thickness due to viscous diffusion. Unlike the inviscid case in which the fingers continually grow, the viscous and vortical effects eventually remove the driving instability and surface tension pulls the interface back. The motion as the interface contracts is complex and it is unclear whether or not it would pinch off at longer times. The question of how viscous and vortical effects affect the interfacial dynamics for much larger We for which the the invscid vortex sheet collapses during roll-up is also open. These two questions are the central themes of the numerical investigation of this present work.

Numerical simulations of sheared flows including viscous, vortical, and surface tension effects are quite challenging. They require the solution of the incompressible Navier-Stokes equations in the presence of a free surface. Because surface tension can play such a crucial role in the flow dynamics, it is essential that tension forces and geometric quantities such as interfacial curvature be computed very accurately. At the same time, the flow must be well resolved globally but due to the surface concentration of high vorticity and the sharp flow variations across the free surface, this can be a daunting task. Furthermore, capturing the true regularizing effects of viscosity and surface tension for large We and Reynolds number can be expected to be difficult due to the underlying ill-posedness of the inviscid $We = \infty$ problem.

Because of the need to compute accurately interfacial quantities, it seems natural to

employ a numerical method in which the fluid interface is explicitly tracked rather than "captured" on a fixed grid. Among the most popular front-tracking methods for multi-phase flow, which use an Eulerian grid for the fluid flow together with a lower-dimensional grid to track the interface, are the method developed by Glimm and collaborators[14–16], the Immersed Boundary Method introduced by Peskin[17], and the related method proposed by Unverdi and Tryggvason[18]. One of the main difficulties of front-tracking methods is the problem of coupling the fixed Eulerian grid for the fluid flow with the interface dynamics. One approach is to use one-sided "ghost cell" extrapolation around the front as done in Glimm's method. An alternative, implementationally easier, approach is to replace the sharp interface by an interface of finite thickness, typically a few mesh points. In this diffused-interface approach, used by the Immersed Boundary and some closely related methods, interfacial quantities such as tension forces, are spread continuously within the interface layer so that they can be prolonged to the fixed Eulerian grid. While conceptually simple, the diffused-interface approach requires very high spatial resolution in a vicinity of the interface to allow the use of sufficiently thin layers and avoid excessive numerical diffusion.

Another well-known problem that has plagued front-tracking methods for multi-phase flows is the tension-induced numerical stiffness[19–21]. Indeed, the spatial derivatives introduced by interfacial tension forces and the excessive marker (particle) clustering characteristic of Lagrangian front-tracking lead to prohibitively small time steps for explicit methods. A partial remedy for this problem has been mesh re-distribution done by point insertion and deletion. This process has however the drawback of introducing strong artificial smoothing as a result of repeated interpolation. An effective alternative is to use a suitably chosen tangential velocity for the interface markers to control their distribution. This idea is a key ingredient in the successful non-stiff boundary integral method developed by HLS[20] and has been used recently to relax time-stepping in a hybrid level set-front tracking method for multi-phase flows[22].

To conduct the numerical investigation of the long-time dynamics of a sheared interface, we develop a non-stiff fully adaptive immersed boundary-type method that overcomes the aforementioned difficulties. This novel method marries the two main approaches for mesh adaption, moving meshes (dynamic interfacial parametrizations as constructed in Refs. 12,20) and adaptive mesh refinements, and combines them with an efficient predictor-corrector discretization to remove the surface tension-induced stability constraint for the

Weber numbers of interest. As a result, we obtain a robust fully adaptive method with only a first order CFL condition for a wide range of Weber numbers. We focus our investigation on long-time flow dynamics and on intermediate and large We flow for which interface fingering and roll-up occur. To assess the importance of the viscous and vortical effects in the interfacial dynamics the full viscous flow simulations are compared when appropriate with inviscid counterparts computed with the boundary integral method developed by HLS[20].

Our numerical study begins with the investigation of the viscous and vortical effects on the roll-up motion for which there is an interface collapse in the inviscid case. For small but finite viscosity ($Re = O(10^4)$) we find that well past the inviscid topological singularity time disparate parts of the interface come in close proximity during roll-up but the interface surprisingly escapes reconnection. Fixing We, we examine the flow behavior as Re is increased and find evidence that suggests a topological singularity will only occur in the limit $Re \to \infty$, for the initial data we consider. Following the study of the roll-up motion we look at the dynamics of the sheared interface at an intermediate Weber number for which elongated interpenetrating fingers of fluid develop. We find that the Kelvin-Helmholtz instability weakens due to shedding of vorticity and unlike the inviscid counterpart in which there is indefinite finger growth the viscous interface is pulled back by surface tension just as reported in Ref. 13 . Then a striking motion occurs; as the interface recedes, thin necks connecting pockets of fluid with the rest of the fingers form. Narrow jets are observed at the necking regions but the vorticity there ultimately appears to be insufficient to drain all the fluid and cause reconnection. However, at another point, two disparate portions of the interface come in close proximity as the interface continues to contract. Large curvature points and an intense concentration of vorticity are observed in this thinning region and then the motion is abruptly terminated by the collapse of the interface. Finally, motivated by the suggestion of HLS[12] that the formation of thin jet may be the leading mechanism for topological reconnection in the 2D inviscid flow, we look at the dynamics of an isolated jet between two disjoint interfaces. In this case, for a special set of initial conditions, we find that the increase of vorticity concentration at necking points is sustained and becomes high enough to drain the fluid and lead to a clear interface collapse.

The rest of the paper is organized as follows. The governing equations are given in Section II and a detailed description of the non-stiff fully adaptive method is provided in Section III. The results of the numerical study are presented in Section V. Further discussion

and concluding remarks are given in Section VI.

II. THE GOVERNING EQUATIONS

A. The Viscous flow

We consider the flow of two immiscible, density and viscosity matched incompressible fluids separated by a sheared interface subjected to constant surface tension. The flow takes place in a two-dimensional channel, periodic in the streamwise direction and whose walls move in opposite directions. The governing equations are the incompressible Navier-Stokes equations which, treating *both* the fluid interface and the walls as massless *immersed boundaries*, can be written as:

$$\rho \left\{ \frac{\partial}{\partial t}\mathbf{u}(\mathbf{x},t) + [\mathbf{u}(\mathbf{x},t)\cdot\nabla]\,\mathbf{u}(\mathbf{x},t) \right\} + \nabla p(\mathbf{x},t) \;=\; \mu\,\Delta\mathbf{u}(\mathbf{x},t) + \mathbf{f}(\mathbf{x},t), \tag{1}$$

$$\nabla\cdot\mathbf{u}(\mathbf{x},t) \;=\; 0, \tag{2}$$

where $\mathbf{u}(\mathbf{x},t)$ and $p(\mathbf{x},t)$ are the velocity field and the pressure respectively at each point $(\mathbf{x},t)$ within the channel and for $t \geq 0$. The mass density ρ and the viscosity coefficient μ are both assumed to be constant.

The driving force $\mathbf{f}(\mathbf{x},t)$ in (1) contains a singularly supported term due to surface tension which enforces the following *dynamic* jump condition at the fluid interface Γ

$$-[p]_\Gamma + \mu\hat{\mathbf{n}}\cdot[\nabla\mathbf{u} + \nabla\mathbf{u}^T]_\Gamma\cdot\hat{\mathbf{n}} = -\tau\kappa, \tag{3}$$

where $[\cdot]_\Gamma$ denotes the jump accross the interface, $\hat{\mathbf{n}}$ is the outward unit normal, τ is the (constant) surface tension coefficient, and κ is the local mean curvature. For $\mu \neq 0$, the velocity field $\mathbf{u}$ is continuous at the fluid interface, i.e. $[\mathbf{u}]_\Gamma = 0$. Continuitiy of the velocity across Γ and incompressibility can be used to reduce (3) to the Laplace-Young condition:

$$[p]_\Gamma = \tau\kappa. \tag{4}$$

Kinematically interfacial Lagrangian particles are only required to move with the normal velocity of the fluid; their tangential velocity can be arbitrarily choosen as we will discuss later.

In the tradition of the immersed boundary method, the walls are also modeled as infinitely thin massless immersed boundaries and as such they add a contribution to $\mathbf{f}(\mathbf{x},t)$. In

the absence of any other external forces to drive the flow, $\mathbf{f}(\mathbf{x},t)$ is given by the singular distribution

$$\mathbf{f}(\mathbf{x},t) = \int_{\mathrm{I}} \tau \frac{\partial \hat{\mathbf{t}}}{\partial \alpha} \delta(\mathbf{x} - \mathbf{X}(\alpha,t))\, d\alpha + \int_{\mathrm{W}} \mathbf{F}_{\mathrm{W}}(\alpha,t)\delta(\mathbf{x} - \mathbf{X}(\alpha,t))\, d\alpha\,, \tag{5}$$

where $\delta(\cdot)$ is the two-dimensional Dirac delta and $\hat{\mathbf{t}}$ is the unit tangent at the fluid interface. Here $\mathbf{X}(\alpha,t)$ represents a parametrization at time t of *both* the fluid interface ($\alpha \in I$) and the walls ($\alpha \in W$), with α being the Lagrangian parameter (marker label). The subscripts in the integrals denote integration on the fluid interface ("I") and on the walls ("W"). Assuming that *tethers* connect wall to anchor points $\mathbf{X}_{\mathrm{W}}(\alpha,t)$ whose evolution in time is known in advance, the force on the walls $\mathbf{F}_{\mathrm{W}}$ is suitably modeled by

$$\mathbf{F}_{\mathrm{W}}(\alpha,t) = -S(\alpha)\left[\mathbf{X}(\alpha,t) - \mathbf{X}_{\mathrm{W}}(\alpha,t)\right], \qquad \alpha \in W, \tag{6}$$

where $S(\alpha)$ is the stiffness defined on the link between wall and anchor points. Since lower and upper walls move in streamwise direction with uniform velocities $(U_1, 0)$ and $(U_2, 0)$, $U_1 > 0 > U_2$, respectively, the position of anchor points at time t is given by

$$\mathbf{X}_{\mathrm{W}}(\alpha,t) = \mathbf{X}_{\mathrm{W}}(\alpha,0) + t\,(U_i, 0)\,, \quad t \geq 0, \quad i = 1,2, \quad \alpha \in W. \tag{7}$$

The motion of the anchor points imposes the desired movement to wall points by "dragging" them through the fluid. Alternatively, this wall-fluid interaction can be also modeled with simple slip boundary conditions on fixed walls.

Finally, the immersed boundaries move with the local (continuous) fluid velocity:

$$\frac{\partial}{\partial t}\mathbf{X}(\alpha,t) = \int_{\Omega} \mathbf{u}(\mathbf{x},t)\delta(\mathbf{x} - \mathbf{X}(\alpha,t))\, d\mathbf{x}\,, \;\; \alpha \in \mathrm{I} \cup \mathrm{W}\,. \tag{8}$$

We define the length scale λ as the periodicity length of the channel and the velocity scale U as the difference between the horizontal velocities at the walls. The flow can be described by two dimensionless groups, the Weber number We and the Reynolds number Re, given by

$$We = \frac{\rho \lambda U^2}{\tau} \qquad \text{and} \quad Re = \frac{\rho \lambda U}{\mu}. \tag{9}$$

B. The inviscid vortex sheet model

We consider two infinite two-dimensional layers of inviscid, incompressible, irrotational, and immisible density-matched fluids separated by a sharp interface Γ whose position at

time t is given in parametric form by $\mathbf{X}(\alpha,t) = (X(\alpha,t), Y(\alpha,t))$, with α in $[0,1]$. At this fluid interface the following boundary conditions are imposed:

$$[\mathbf{u}]_\Gamma \cdot \hat{\mathbf{n}} = 0, \tag{10}$$

$$[p]_\Gamma = \tau\kappa, \tag{11}$$

where $[\cdot]_\Gamma$ denotes the jump across the interface and again p, τ, and κ are the pressure, the surface tension, and the mean curvature respectively. The kinematic condition (10) is the usual requirement that particles on the surface, remain there. Condition (11) is Laplace-Young condition introduced before. The tangential fluid velocity at Γ is usually discontinuous and the model is called a *vortex sheet*. Introducing the complex position variable $Z(\alpha,t) = X(\alpha,t) + iY(\alpha,t)$, we can write a boundary integral formulation for the interface evolution equations in the dimensionless form[12]:

$$\frac{\partial Z}{\partial t} = W^* + \frac{Z_\alpha}{|Z_\alpha|}U_A, \tag{12}$$

$$\frac{\partial \gamma}{\partial t} = \frac{\partial}{\partial \alpha}\left(\frac{U_A\gamma}{|Z_\alpha|}\right) + \frac{1}{We}\kappa_\alpha, \tag{13}$$

where γ is the (unnormalized) vortex sheet strength which measures the discontinuity in the tangential component of the fluid velocity. The complex interfacial velocity W, assuming 1-periodicity, is given by Birkhoff-Rott integral:

$$W(\alpha,t) = \frac{1}{2}\,\text{P.V.}\int_0^1 \gamma(\alpha',t)\cot\pi(Z(\alpha,t) - Z(\alpha',t))d\alpha', \tag{14}$$

where P.V. stands for the principal value integral and the asterisk in (12) denotes the complex conjugate. In (12) and (13), $U_A(\alpha,t)$ is an arbitrary tangential velocity that determines the frame or parametrization of the fluid interface. The freedom in selecting U_A has been exploited by HLS to design a class of efficient *non-stiff* boundary integral methods. Here we will transfer this idea to the immersed boundary method setting (see Section III A 1).

The dimensionless Weber number is again given by $We = \rho\lambda U^2/\tau$. In order to have equivalent Weber numbers for both the viscous and the inviscid models we choose the velocity scale U for the inviscid vortex sheet to be $2U_\infty$, where $(\pm U_\infty, 0)$ is the limiting fluid velocity as $y \to \infty$. The average value, $\bar{\gamma}$, of γ over one period in α satisfies $-\bar{\gamma}/2 = U_\infty$ and thus in dimensionless variables $\bar{\gamma} = -1$. Note that $\bar{\gamma}$ is time-invariant. We use this property to define the velocity of the viscous fluid (Section II A) at the channel wall as $\pm U_\infty = \mp\bar{\gamma}/2 = \pm 1/2$.

III. A FULLY ADAPTIVE NON-STIFF NUMERICAL METHOD

Immersed boundary-type methods combine an Eulerian representation of the fluid flow with a Lagrangian "marker" evolution of the immersed interfaces, as shown schematically in Figure 1. Tracking separately the location of the fluid interface with a Lagrangian mesh allows accurate computation of fluid interface position, geometric quantities, and interfacial forces. However, as it is well-known, Lagrangian front-tracking suffers from excessive marker (particle) clustering that leads to poor overall resolution and above all prohibitively small time steps.

Another common element of immersed boundary-type methods is the use of singularly supported (δ) forces to conveniently account for the interfacial dynamic jump conditions. Numerically, these localized forces are spread a few mesh points by using a mollified approximation to the δ distribution that retains the main weight on the (immersed) interface. This results in a diffused-interface model in which the originally sharp fluid interface is replaced by transition regions of the order of the mesh size. Across these regions sharp flow gradients and vorticity concentration typically occur. Consequently, to accurately compute flow quantities and to avoid numerical effects very high resolution *must* be employed around the immersed boundaries.

To overcome the aforementioned difficulties associated with Lagrangian tracking and the surface tension-induced stability constraint, and to efficiently resolve the flow in a vicinity of the fluid interface as well as globally we propose a fully adaptive non-stiff method. Our computational strategy has three main components: dynamically adaptive tracking of the fluid interface in the form of marker equi-distribution, a semi-implicit predictor-corrector time marching scheme, and adaptive mesh refinements to accurately resolve flow quantities, particularly in a vicinity of the interface. We describe next each of the three ingredients along with the spatial discretization we employ. The complete algorithm is summarized in Appendix A as a reference. The overall method is second order accurate in space and time for smooth solutions but due to the interface smearing, charecteristic of the IB method, it has only first order spatial accuracy for sharp interface problems.

A. Relaxing the surface tension-induced stability constraint

1. *Dynamic Lagrangian equi-distribution*

Excessive marker clustering is a well-known problem in tracking methods. The most common remedy to this problem has been regridding or particle redistribution by point insertion and deletion. However, this approach has the drawback of introducing strong smoothing to the fluid interface as a result of repeated interpolation.

In the context of boundary integral methods, HLS[20] have proposed a very effective alternative approach to control particle distribution. The idea is to use the freedom in selecting the tangential velocity of the interface markers to control their distribution at all times. Indeed, kinematically the markers are only required to move with the normal velocity of the fluid. Thus (8) could be changed to:

$$\mathbf{X}_t(\alpha,t) = \int \mathbf{u}(\mathbf{x})\delta(\mathbf{x}-\mathbf{X}(\alpha,t))d\mathbf{x} + U_A(\alpha,t)\hat{\mathbf{t}} =: \mathbf{U}(\alpha,t) + U_A(\alpha,t)\hat{\mathbf{t}}, \tag{15}$$

where $U_A(\alpha,t)$ is arbitrary and determines the frame or parametrization used to describe the interface. For example, a U_A can be found to cluster interface markers in a controlled fashion in regions of high curvature[12] or to keep the markers equi-distributed. Here we opt for the latter as we expect the fluid interface to be globally deformed. If the markers are equi-distributed initially the following choice of U_A keeps them equi-distributed at all times[20]:

$$U_A(\alpha,t) = -U_T(\alpha,t) + \int_0^\alpha [s_\alpha \kappa U_N - < s_\alpha \kappa U_N >] d\alpha', \tag{16}$$

where $U_T = \mathbf{U}\cdot\hat{\mathbf{t}}$, $U_T = \mathbf{U}\cdot\hat{\mathbf{t}}$, $s_\alpha = \sqrt{X_\alpha^2 + Y_\alpha^2}$ is the arc-length metric, κ is the mean curvature, and $< \cdot >$ stands for the spatial mean over one spatial period. At the walls, we simply take $U_A \equiv 0$.

2. *Predictor-corrector semi-implicit strategy*

We employ a semi-implicit strategy to remove the highest order stability constraint in the equations of motion. We write this non-stiff discretization in the form of an efficient second order predictor-corrector scheme which stems from a general iterative implicit discretization. For simplicity, we describe the scheme assuming a constant time step Δt and equal mesh spacing $\Delta x = \Delta y = h$.

Typically, a time step to go from time level t^n to time level t^{n+1} starts by employing (7) to move wall-anchor points. After this, one performs:

(i) *Predictor step*

From computed values $\mathbf{u}^n$, $p^{n-\frac{1}{2}}$, and $\mathbf{X}^n$ for the velocity, pressure, and immersed boundary position respectively, known from the previous time step, obtain *predicted values* $\mathbf{u}^{n+1,1}$ and $\mathbf{X}^{n+1,1}$ for the new velocity field and immersed boundary position at time $t = t^{n+1}$ by solving

$$\frac{\mathbf{u}^{*,1} - \mathbf{u}^n}{\Delta t} + \frac{\mathbf{G}\, p^{n-\frac{1}{2}}}{\rho} = \frac{\mu}{\rho} L\,(\frac{\mathbf{u}^{*,1} + \mathbf{u}^n}{2}) - [(\mathbf{u}\cdot\nabla)\mathbf{u}]^n + \frac{\mathbf{f}}{\rho}^n, \tag{17}$$

$$\frac{\mathbf{u}^{n+1,1} - \mathbf{u}^n}{\Delta t} + \frac{\mathbf{G}\, p^{n+\frac{1}{2},1}}{\rho} = \frac{\mathbf{u}^{*,1} - \mathbf{u}^n}{\Delta t} + \frac{\mathbf{G}\, p^{n-\frac{1}{2}}}{\rho}, \tag{18}$$

$$\mathbf{D}\cdot\mathbf{u}^{n+1,1} = 0, \tag{19}$$

$$\begin{aligned}\frac{\mathbf{X}^{n+1,1} - \mathbf{X}^n}{\Delta t} = \frac{h^2}{2}\sum_{\mathbf{x}} \Big(\mathbf{u}^{n+1,1}\delta_h(\mathbf{x}-\mathbf{X}^n) \,+\, \mathbf{u}^n\delta_h(\mathbf{x}-\mathbf{X}^n)\Big) \\ + \frac{1}{2}(U_A^{n+1,1}\hat{\mathbf{t}}^n + U_A^n\hat{\mathbf{t}}^n)\,,\end{aligned} \tag{20}$$

where

$$\hat{\mathbf{t}}^n = \frac{\mathrm{D}_{\Delta\alpha}\mathbf{X}^n}{\|\mathrm{D}_{\Delta\alpha}\mathbf{X}^n\|}, \tag{21}$$

and $\mathrm{D}_{\Delta\alpha}$ is the centered difference operator in α. Note that, as customary in projection methods, a provisional velocity field $\mathbf{u}^*$ is obtained from (17), and then, using (18) and (19), it is projected onto the divergence-free vector field space. L, $\mathbf{G}$ and $\mathbf{D}$ are standard second order finite difference Laplacian, gradient and divergence operators defined on a staggered grid and will be given in Section III B.

(ii) *Corrector step*

Once predicted values are available, they are utilized to compute approximations to the nonlinear and to the singular force terms at $t = t^{n+\frac{1}{2}}$ (using linear interpolation) and another projection is performed to obtain *corrected values* $\mathbf{u}^{n+1,2}$ and $\mathbf{X}^{n+1,2}$ as

follows:

$$\frac{\mathbf{u}^{*,2}-\mathbf{u}^n}{\Delta t}+\frac{\mathbf{G}\,p}{\rho}^{n+\frac{1}{2},1}=\frac{\mu}{\rho}L\,(\frac{\mathbf{u}^{*,2}+\mathbf{u}^n}{2})-[(\mathbf{u}\cdot\nabla)\mathbf{u}]^{n+\frac{1}{2},1}+\frac{\mathbf{f}}{\rho}^{n+\frac{1}{2},1}, \tag{22}$$

$$\frac{\mathbf{u}^{n+1,2}-\mathbf{u}^n}{\Delta t}+\frac{\mathbf{G}\,p}{\rho}^{n+\frac{1}{2},2}=\frac{\mathbf{u}^{*,2}-\mathbf{u}^n}{\Delta t}+\frac{\mathbf{G}\,p}{\rho}^{n+\frac{1}{2},1}, \tag{23}$$

$$\mathbf{D}\cdot\mathbf{u}^{n+1,2}=0, \tag{24}$$

$$\begin{aligned}\frac{\mathbf{X}^{n+1,2}-\mathbf{X}^n}{\Delta t}=&\frac{h^2}{2}\sum_{\mathbf{x}}\Big(\mathbf{u}^{n+1,2}\delta_h(\mathbf{x}-\mathbf{X}^{n+1,1})\;+\;\mathbf{u}^n\delta_h(\mathbf{x}-\mathbf{X}^n)\Big)\\&+\frac{1}{2}(U_A^{n+1,2}\hat{\mathbf{t}}^{n+1,1}+U_A^n\hat{\mathbf{t}}^n)\,,\end{aligned} \tag{25}$$

where

$$[(\mathbf{u}\cdot\nabla)\mathbf{u}]^{n+\frac{1}{2},1}=\frac{1}{2}\{\,[(\mathbf{u}\cdot\nabla)\mathbf{u}]^{n+1,1}+[(\mathbf{u}\cdot\nabla)\mathbf{u}]^n\,\}, \tag{26}$$

$$\mathbf{f}^{n+\frac{1}{2},1}=\frac{1}{2}(\,\mathbf{f}^{n+1,1}+\mathbf{f}^n\,)\,. \tag{27}$$

The predicted force and tangent vector are computed by

$$\mathbf{f}^{n+1,1}=\Delta\alpha\sum_{k\in\,\mathrm{I}}\tau\mathrm{D}_{\Delta\alpha}\hat{\mathbf{t}}_k^{n+1,1}\delta_h(\mathbf{x}-\mathbf{X}_k^{n+1,1})+\sum_{k\in\,\mathrm{W}}\mathbf{F}_{W,k}^{n+1,1}\delta_h(\mathbf{x}-\mathbf{X}_k^{n+1,1})\,, \tag{28}$$

$$\hat{\mathbf{t}}^{n+1,1}=\frac{\mathrm{D}_{\Delta\alpha}\mathbf{X}^{n+1,1}}{\|\mathrm{D}_{\Delta\alpha}\mathbf{X}^{n+1,1}\|}, \tag{29}$$

where $\Delta\alpha$ is the mesh spacing in the parametrizing variable. A standard second order discretization is used to approximate U_A, the added tangential velocity (16). $U_A^{n+1,1}$ is computed employing $\mathbf{u}^{n+1,1}$ and $\mathbf{X}^n$ and in the corrector step $U_A^{n+1,2}$ is obtained using $\mathbf{u}^{n+1,2}$ and $\mathbf{X}^{n+1,1}$.

The corrected values $\mathbf{u}^{n+1,2}$ and $\mathbf{X}^{n+1,2}$ are the numerical solution at the end of the time step $t=t^{n+1}$, i.e., $\mathbf{u}^{n+1}:=\mathbf{u}^{n+1,2}$ and $\mathbf{X}^{n+1}:=\mathbf{X}^{n+1,2}$.

The predictor-corrector method (17)–(29) originates from the more general iterative scheme given in Appendix B. When iterated to convergence, the scheme corresponds to the (implicit) Crank-Nicolson discretization.

The overall scheme introduced here is a variation of the implicit Immersed Boundary Method proposed by Roma, Peskin, and Berger[23]. Besides the Lagrangian mesh adaption, a complete new feature, the main difference is in the manner we compute the non-linear term, here being fully implicit in time. It is interesting to note that for the range of Weber numbers

we tested, $10 \leq We$, the predictor-corrector scheme in combination with the dynamic equidistribution removes the time stepping constraint associated with surface tension.

Observe that in the predictor-corrector scheme (17)-(25), the Dirac's delta distribution is approximated by a mollified version δ_h. There are many possible choices for this function. Here, we choose Peskin's delta[17]:

$$\delta_h(\boldsymbol{x}_{i,j}) = d_h(x_i)\, d_h(y_j)\,, \tag{30}$$

where

$$d_h(z) = \begin{cases} 0.25\,[1+\cos(\frac{\Pi}{2}\, z/h)]/h & \text{for } |z| < 2h, \\ 0 & \text{for } |z| \geq 2h. \end{cases} \tag{31}$$

This choice for $\delta_h(\mathbf{x})$ provides good regularization properties around the interface and it is motivated by a set of compatibility properties described by Peskin[17]. Alternative discretizations can be found in Refs. 23,24.

It is well known, see for example[25], that the immersed boundary setting produces small amplitude mesh-scale oscillations in the interface position. When derivatives are computed from the interface position to obtain geometric quantities and tension forces, these oscillations are amplified by numerical differentiation and if left unattended could lead to numerical instability. To eliminate the growth of the small amplitude mesh-scale oscillations characteristic of immersed boundary-based methods, we apply the fourth order filter[26]:

$$\mathbf{X}_k \leftarrow \frac{1}{16}(-\mathbf{X}_{k-2} + 4\mathbf{X}_{k-1} + 10\mathbf{X}_k + 4\mathbf{X}_{k+1} - \mathbf{X}_{k+2}). \tag{32}$$

The filter is applied every 10 time steps to the fluid interface markers and every time step on the wall markers. The effect of the filter on the numerical solution was tested with a resolution study and by changing the frequency at which the filter was applied from every 10 to every 100 time steps. No appreaciable difference was found except for the more sensitive case of zero surface tension ($We = \infty$) and high Reynolds number.

B. Spatial discretization

In the projection method we use here, we place the numerical approximations of the Eulerian variables, $\mathbf{u}_{ij}$ and p_{ij}, in a staggered fashion on the computational (composite) mesh. The pressure is computed at the cell centers which are indexed by (i, j). The velocity

is discretized at the cell edges as $\mathbf{u}_{ij} := (u_{i-\frac{1}{2},j},\, v_{i,j-\frac{1}{2}})$. Figure 1 shows the location of the variables for a uniform mesh patch.

In what follows, time indices are suppressed in favor of clarity. For the velocity and pressure fields located as explained previously, the divergence and gradient operators are approximated by the second order finite difference operators

$$(\mathbf{D}\cdot\mathbf{u})_{i,j} \;=\; \frac{u_{i+\frac{1}{2},j}-u_{i-\frac{1}{2},j}}{h}+\frac{v_{i,j+\frac{1}{2}}-v_{i,j-\frac{1}{2}}}{h}, \tag{33}$$

$$(\mathbf{G}\,p)_{i,j} \;=\; \left(\frac{p_{i,j}-p_{i-1,j}}{h},\,\frac{p_{i,j}-p_{i,j-1}}{h}\right). \tag{34}$$

The discretization of the viscous terms in (1) is given by the 5-point stencil

$$(L\,\boldsymbol{u})_{i,j} = \left(\frac{u_{i+\frac{1}{2},j}+u_{i-\frac{3}{2},j}+u_{i-\frac{1}{2},j+1}+u_{i-\frac{1}{2},j-1}-4u_{i-\frac{1}{2},j}}{h^2},\right.$$

$$\left.\frac{v_{i,j+\frac{1}{2}}+v_{i,j-\frac{3}{2}}+v_{i+1,j-\frac{1}{2}}+v_{i-1,j-\frac{1}{2}}-4v_{i,j-\frac{1}{2}}}{h^2}\right), \tag{35}$$

which can also be denoted as $(L\,\boldsymbol{u})_{i,j} = ((L\,u)_{i-\frac{1}{2},j},\,(L\,v)_{i,j-\frac{1}{2}})$.

The nonlinear term, $[(\mathbf{u}\cdot\nabla)\mathbf{u}]$, is approximated by the non-conservative second order centered scheme (see for example[27])

$$\begin{aligned}[(\boldsymbol{u}\cdot\nabla)\boldsymbol{u}]_{i,j} \;\approx\; \Bigg(&u_{i-\frac{1}{2},j}\Big(\frac{u_{i+\frac{1}{2},j}-u_{i-\frac{3}{2},j}}{2h}\Big)+\overline{v}_{i-\frac{1}{2},j}\Big(\frac{u_{i-\frac{1}{2},j+1}-u_{i-\frac{1}{2},j-1}}{2h}\Big),\\ &\overline{u}_{i,j-\frac{1}{2}}\Big(\frac{v_{i+1,j-\frac{1}{2}}-v_{i-1,j-\frac{1}{2}}}{2h}\Big)+v_{i,j-\frac{1}{2}}\Big(\frac{v_{i,j+\frac{1}{2}}-v_{i,j-\frac{3}{2}}}{2h}\Big)\Bigg),\end{aligned} \tag{36}$$

where

$$\begin{aligned}\overline{v}_{i-\frac{1}{2},j} \;&=\; \frac{v_{i,j-\frac{1}{2}}+v_{i,j+\frac{1}{2}}+v_{i-1,j+\frac{1}{2}}+v_{i-1,j-\frac{1}{2}}}{4},\\ \overline{u}_{i,j-\frac{1}{2}} \;&=\; \frac{u_{i-\frac{1}{2},j}+u_{i-\frac{1}{2},j-1}+u_{i+\frac{1}{2},j-1}+u_{i+\frac{1}{2},j}}{4}.\end{aligned}$$

C. Adaptive mesh refinements

In the fully adaptive computational scheme, regions of the flow bearing special interest are covered by block-structured grids, defined as a hierarchical sequence of nested, progressively finer levels (composite grids). Each level is formed by a set of disjoint rectangular grids. Ghost cells are employed around each grid, for all the levels, and underneath fine grid patches

to formally prevent the finite difference operators from being redefined at grid borders and at interior regions which are covered by finer levels. Values defined in these cells are obtained from interpolation schemes, usually with second or third order accuracy, and not from solving the equations of the problem. The description of composite grids is given in Ref. 28 in greater detail. Figure 2 shows an interface between two successive refinement levels, and the location of coarse and fine variables.

Composite grid generation depends on a *flagging step*, that is, on determining first the cells whose collection gives the region where refinement is to be applied. Here, we mark for refinement a neighborhood of all immersed boundary points (*immersed boundary uniform covering*). We also flag points at which vorticity (in absolute value) is at least 30% the global vorticity maximum. Once the collection of flagged cells is obtained, grids in each level are generated by applying the algorithm for point clustering due to Berger and Rigoutsos[29]. Regridding is performed as often as an immersed boundary point gets "too close" to the interface of the finest level.

It is important to comment that the refinement ratio is equal to two, and that we employ multilevel-multigrid methods to solve for both the provisional vector fields, $\mathbf{u}^{*,m}$, in the parabolic step of the projection method, and for the pressure $p^{n+\frac{1}{2},m}$, in its elliptic step ($m = 1, 2$). V-cycles are employed with one relaxation on each multigrid level, upwards and downwards. Detailed descriptions of the methodology to solve for the pressure can be found in Refs. 23,30.

Projection methods on locally refined meshes, based on cell centered discretizations of all variables, were first proposed by Howell[31]. Minion[32,33] developed a second order *approximate* projection method that fascilitated the implementation of the multilevel-multigrid methods. The projection method we employ here[23] is based on Minion's intermediate projection step on locally refined staggered grids.

IV. BOUNDARY INTEGRAL DISCRETIZATION FOR THE INVISCID SHEET

To solve numerically the vortex sheet equations (12)-(14) we use the method introduced by HLS[12,20]. For completeness, we outline the method next. For a detailed description the reader is referred to Refs. 12,20.

The method is based on the reformulation of the equations of motion in terms of the

tangent angle θ to the interface and the arc-length metric $s_\alpha = \sqrt{X_\alpha^2 + Y_\alpha^2}$ which are variables more naturally related to the curvature. It also identifies the small scale terms that contribute to the surface tension-induced stiffness. The evolution equation (12) in the new variables becomes,

$$\frac{\partial s_\alpha}{\partial t} = (U_T + U_A)_\alpha - \theta_\alpha U_N, \tag{37}$$

$$\frac{\partial \theta}{\partial t} = \frac{1}{s_\alpha}[U_{N\alpha} + (U_T + U_A)\theta_\alpha], \tag{38}$$

where U_N and U_T are the normal and tangential components of the interfacial fluid velocity respectively and the particular U_A given by (16) is selected.

The stiffness is hidden at the small spatial scales of $U_{N\alpha}$ in the θ-equation. The leading order behavior of U_N at small scales is given by[20],

$$U_N(\alpha, t) \sim \frac{1}{2s_\alpha}\mathcal{H}[\gamma](\alpha, t), \tag{39}$$

where $\mathcal{H}$ is the Hilbert transform. In the equi-distributed frame s_α is constant is space and the inviscid vortex sheet equation of motion can be written as

$$\frac{ds_\alpha}{dt} = \int_0^1 \theta_{\alpha'} U_N d\alpha', \tag{40}$$

$$\frac{\partial \theta}{\partial t} = \frac{1}{2s_\alpha^2}\mathcal{H}[\gamma_\alpha] + P, \tag{41}$$

$$\frac{\partial \gamma}{\partial t} = \frac{1}{We}\frac{1}{s_\alpha}\theta_{\alpha\alpha} + Q, \tag{42}$$

where P represents lower-order terms at small spatial scales. To remove the stiffness it is sufficient to discretize implicitly the leading order in (41)-(42) and treat the lower order terms P and Q explicitly. We use the SBDF fourth-order explicit/implicit multi-step method in Ref.34. The principal value integral is approximated with the spectrally accurate alternate-point trapezoidal rule[6] and each spatial derivative and the Hilbert transform are computed pseudo-spectrally, i.e. using the discrete Fourier transform. The implementation we use here has been tested and validated with several examples in Ref. 35 where also the convergence of the method was rigorously established.

V. RESULTS

For high Reynolds numbers, we expect the initial K-H instability to be well predicted by the linear stability analysis for the inviscid case. This is supported by the growth estimates

based on viscous potential flow theory by Funada and Joseph[36]. According to the inviscid linear stability analysis, the dispersion relation gives instability for wave numbers $0 < |k| < We/4\pi$ (see for example[12]). Thus, for sufficiently small We (e.g. $We = 10$) there would be no unstable modes and the initially flat interface would undergo a simple wave-like motion as documented in Ref. 12 for the inviscid sheet. We found the same type of motion for the corresponding viscous interface. We do not report on this case here but instead direct our attention to larger Weber numbers, $We = 50$, 200, and 400.

A. Initial conditions

We focus on the initial conditions used by Krasny[4] and by HLS[12] in their study of an inviscid vortex sheet. These initial conditions correspond to a perturbation of a flat sheet with a uniformly concentrated vorticity distribution. The nonlinear motion of the inviscid vortex sheet with these initial conditions has been well studied both with and without surface tension[4,6,12].

The initial fluid interface $\mathbf{X}_0$ is given in parametric form by

$$\mathbf{X}_0(\alpha) = (\alpha + 0.01 \sin 2\pi\alpha, -0.01 \sin 2\pi\alpha) \tag{43}$$

for $0 \leq \alpha \leq 1$. We obtain the initial velocity (u_0, v_0) from a delta supported vorticity with unit strength:

$$\omega_0(x, y) \;=\; \delta_h(\phi(x, y)), \tag{44}$$

$$\phi(x, y) \;=\; y + 0.01 \sin 2\pi(x + y), \tag{45}$$

for (x, y) in our computational domain $\Omega_C = [0, 1] \times [-1, 1]$ and with δ_h given by (31). Note that the zero level set of ϕ is precisely the initial curve specified by (43). Given this vorticity distribution, we first find the *stream function* $\psi(\mathbf{x})$ by solving numerically (with standard second order finite differences) the Poisson's equation

$$\Delta\psi = -\omega_0, \tag{46}$$

in Ω_C with periodic boundary conditions in the streamwise direction and Dirichlet homogeneous conditions in the normal-wall direction. We then compute the initial velocity from ψ

via

$$u_0(\mathbf{x}) = +\frac{\partial \psi}{\partial y}(\mathbf{x}), \tag{47}$$

$$v_0(\mathbf{x}) = -\frac{\partial \psi}{\partial x}(\mathbf{x}), \tag{48}$$

employing centered differences.

For the inviscid vortex sheet model (12)-(14) we take the initial vortex sheet strength as $\gamma = -1$ which corresponds to the initial condition (44) and (45) in the limit as $h \to 0$.

B. Resolutions

The numerical experiments for the viscous flows we report on here use composite AMR meshes with six and seven levels of refinement. We denote these AMR meshes by L6 and L7 respectively. The finest level of L6 and L7, which covers the immersed boundaries at all times, corresponds to the resolution equivalent to that of a 1024×2048 and 2048×4096 uniform mesh, respectively. The coarsest level corresponds to that of a 32×64 uniform mesh and the refinement ratio between consecutive levels is 2. The support ($4h$) of the mollified delta function reduces accordingly when increasing the numbers of refinement levels. For the range of Weber numbers considered, we find that the time-step size required for numerical stability of our method only requires satisfying a linear (CFL) condition, $\|\mathbf{u}\|_\infty \Delta t < h$, independent of We. Typically, $\Delta t = 0.0005$ for L6 and $\Delta t = 0.00025$ for L7 but the time step is varied adaptively based on the (time-dependent) condition $\|\mathbf{u}\|_\infty \Delta t < h$. Initially, the number of markers N_b on the fluid interface is twice the number of grid points in the horizontal direction, i.e. $N_b = 2048$ for L6 and $N_b = 4096$ for L7. We double N_b whenever the total length of the fluid interface doubles. The interface position at the added points is computed using linear interpolation. We tested this strategy by comparing with computations that used a fixed, sufficiently high N_b (4 times number of grid points in the horizontal direction) and found no appreciable difference in the numerical results.

The inviscid vortex sheet boundary integral computations are computed with 1024 equi-distributed interfacial markers and with $\Delta t = 0.00025$.

C. $We = 200$

We consider first the flow corresponding to $We = 200$. This case was studied in great detail by HLS[12] for the inviscid vortex sheet. For $We = \infty$, $Re = \infty$ the vortex sheet corresponding to the initial conditions (43)-(45) develops the Moore curvature singularity at $t_M \approx 0.37$. For $We = 200$ and $Re = \infty$ linear stability analysis gives 16 initially unstable modes and the fastest growing mode is $k = 11$. The numerical study of HLS[12] revealed that for $We = 200$ surface tension regularizes the Moore singularity and then the inviscid interface undergoes a roll-up motion during which pinching is observed at the estimated time $t_p \approx 1.427$. The formation of this topological singularity is surprising because it takes place in a pure planar motion where the azimuthal component of the surface tension force is absent. We examine now how the presence of of small but finite viscosity, $Re = 20000$, affects this highly nonlinear interfacial dynamics.

Figure 3 offers a comparison between the viscous (left column) and the inviscid (right column) interface profiles. The left column also displays the L7 AMR composite mesh structure represented as patches (in different shades) corresponding to each level of refinement. The region shown is only a portion of the actual computational domain $[0, 1] \times [-1, 1]$ for the viscous flow. The remeshing algorithm does not enforce symmetry and thus the AMR composite mesh is generally not symmetric.

At an early time, $t = 0.70$ [Fig. 3(a) and (a')], already a significant difference between the viscous and the inviscid interfacial profiles can be observed at the center of the free boundaries. The inviscid sheet has developed two fingers which are not yet formed in the viscous interface. The dispersive (capillary) waves running outward from the inviscid sheet at $t = 1.0$ and $t = 1.41$ [Fig. 3(b') and (c')] are absent in the corresponding viscous profiles. For this Reynolds number, viscous dissipation is suppressing these short waves. At $t = 1.41$, close to the inviscid pinching time, the viscous interface is smooth and far from self-intersection. However, outside the interface core region the inviscid and the viscous interfaces coincide quite well up to t_p.

An examination of the vorticity field of the sheared interface, shown in Fig. 4, can help us understand the observed differences. Also appearing in Fig. 4 is the scaled interfacial

vorticity (right column):

$$\omega_I(\alpha,t) = h_{\text{finest}} \int_\Omega \omega(\mathbf{x},t)\delta(\mathbf{x}-\mathbf{X}(\alpha,t))\,d\mathbf{x}\,. \tag{49}$$

The scaling factor h_{finest} has been introduced because the initial, discretized, interfacial vorticity has the mesh-dependent value $0.5/h_{\text{finest}}$. Here $h_{\text{finest}} = 1/2048$ for L7.

As Fig. 4(a) shows, at $t = 0.70$, a significant amount of vorticity has been shed off the interface giving rise to the formation of a pair of vortices, both with positive vorticity. The interfacial vorticity, Fig. 4(a'), shows maxima that are attained around the location of the points of maximum curvature and minima that take place in a neighborhood of the interface center. As Fig. 4 (b)-(c) demonstrates, the vortex pair continues to significantly affect the finger development and the subsequent interfacial roll-up.

The evolution of the viscous interface for longer times, well past t_p is depicted in Fig. 5. The fingers first widen and subsequently undergo much deformation during roll-up producing at $t = 3.2$ a neck and the onset of what appears to be capillary waves. The dynamics of the corresponding vorticity is shown in Figs. 6-7. Vorticity is predominantly shed into the bulk phases from the regions of largest interfacial curvature. In particular, due to this tearing and insufficient production of vorticity at the necking region at $t = 3.2$, Fig. 7(c)-(c'), the fluid there cannot be entirely drained. At $t = 3.8$, Fig. 7(d)-(d'), the sheared interface has an "eye" shape similar to that observed in the experiments of Atsavapranee and Gharib[1]. At this time, the interface has developed two points of very high curvature, around approximately $x = 0.4$ and $x = 0.6$ and on which there is a significant accumulation of vorticity as Fig. 7(d') shows. However, the accumulation of vorticity at these points is not sustained as the free surface continues to stretch. The interface at even longer times, $t = 4.23$ and $t = 4.78$, is presented in Fig. 8 while the corresponding vorticity field is shown in Fig. 9. Shedding, transport, and diffusion of vorticity as well as dispersion due to interfacial tension lead to a convoluted interface but one on which there is no indication of an eventual topological reconnection, at least over the times we have computed. Even a small viscosity appears to have prevented pinching.

To assess the resolution of the L7 computations we compare them with those obtained with L6. Fig. 10 shows a comparison of the interfacial profiles for the adaptive L6 and L7 resolutions at the late stage of the motion. Note that the support of the mollified delta function for L7 is half that of L6. This is also so in the spreading of the initial (uniform)

vorticity. Nevertheless, this resolution comparison demonstrates that there is little difference in the interfacial dynamics for L6 and L7 at this We. The comparison provides also evidence that the L7 computations are well resolved. The time history of the smallest interfacial gap computed for both L6 and L7 resolutions is presented in Fig. 11. Note that because of the delta function spreading, a minimum of 4 mesh points is required to resolve a fluid region bounded by interface segments. Even, at the very last computed time, $t = 4.78$, when the interface is highly stretched and some segments of the interface are close to each other, there are over 26 finest grid points to resolve the smallest gap in the L7 AMR mesh.

To continue exploring the possibility of finite-time pinching and to further study the viscous effects, we now look at the dynamics of the viscous interfacial flow as Re is increased for a fixed We. We select now a larger Weber number, $We = 400$, because based on the inviscid vortex sheet computations[12], the roll-up core is expected to be tighter and thus thinner fluid passages (necking regions) might develop.

D. $We = 400$

Figure 12 depicts the evolution of the inviscid vortex sheet for $We = 400$. The motion presents the same generic features as that for $We = 400$ except that the length scale has been reduced as evidenced by the smaller fingers, tighter sheet core, and shorter capillary waves. The inviscid vortex sheet self-intersects at $t_p \approx 0.82$ as reported by HLS[12].

We now look at the viscous flow dynamics for Reynolds numbers $Re = 5000$, $Re = 10000$, and $Re = 20000$.

1. $Re = 5000$

Figure 13 presents the interfacial profile at different times as well as the corresponding composite AMR mesh structure in a region containing the interface. At $t = 0.7$, Fig. 13(a), the free interface is vertical at $x = 0.5$ and there is yet no formation of fingers. Past t_p, wide and smooth fingers develop, Fig. 13(b), and the interface roll-ups into a wide spiral. Each finger tip comes in close proximity to the opposite side of the interface at $t = 2.3$ producing two necking regions. The thinnest neck is formed approximately at 3.07, Fig. 13(e), reaching a value of 7.7×10^{-3}, 15.69 L7 finest grid mesh cells. The necking region then gradually

opens up as the sheared interface continues to roll [Fig. 13(f)]. Figure 14(a) shows a close-up of the AMR mesh in the necking region at $t = 3.07$, when the minimum interfacial separation is achieved. The time history of the neck width appears in Figure 14(b) where we can clearly see that the interface moves away from pinching for $t > 3.07$.

The pronounced viscous effects on the inviscid topological singularity can be seen Fig. 15(b) which presents a comparison of the viscous and inviscid interface profiles around the inviscid collapse time, $t_p \approx 0.82$. Fig. 15(b) compares the L7 and L6 interfaces at the final time $t = 3.5$. The two curves are indistinguishable from one another within plotting resolution.

The vorticity field and the interfacial vorticity are shown in Figs. 16 and 17. Note that very early in the dynamics at $t = 0.7$ the vorticity, initially concentrated on the interface, has been diffused to a wide viscous layer around the center [Fig. 16(a)]. When the fingers develop, Fig. 16(b), the interfacial vorticity increases attaining maximum values at the finger tips. Vorticity is then shed off the tips into the bulk fluid to give rise to the formation of two vortices as shown in Fig. 16(c). The vorticity on these vortices subsequently diffuses and weakens, as the series of pictures in Fig. 17 show. Around $t = 2.3$, Fig. 17(a)(a'), when the two necking regions develop, the vorticity on the interface segments bounding each neck has opposite signs creating effectively a jet in each of the narrow regions. As the fluid in these regions is drained, vorticity intensifies at the necking points until a minimum neck width is attained around $t = 3.07$ [Fig. 17(b)(b')]. The growth of vorticity then saturates and the necking regions begin to open up [Fig. 17(c)(c')].

2. $Re = 10000$

Figure 18 presents the interface evolution for $Re = 10000$. There is now an earlier formation of the fingers and a tighter roll-up core in comparison with the $Re = 5000$ case. As the fingers roll necking regions develop and the width of the regions decreases until a minimum value is reached at $t \approx 2.28$. After this, the bounding interface segments at the neck separate as Fig. 18(f) shows. The minimum neck width is 5×10^{-3} , 10.24 L7 finest grid cells. A close-up of the AMR L7 mesh around the necking region at $t = 2.28$, when the minimum is reached, is shown in Fig. 19(a) while Fig. 19(b) presents a time history of the neck width. Note that the shapes of the fingers when the necking regions are formed and

when the minimum neck width is achieved are very similar to those observed for 5000. A comparison of the viscous and inviscid interface profiles around the inviscid collapse time, $t_p \approx 0.82$, is given at Fig. 20(a) and Fig. 20(b)compares the L6 and L7 resolutions on the interface at the last computed time $t = 2.5$. Again both resolutions give interfacial profiles that coincide quite well.

Figures 21 and 22 illustrate how vorticity is produced, diffused, and transported dynamically. We can observe larger values of interfacial vorticity than those for 5000 but the vorticity dynamics for both flows appears to be very similar. Vorticity shed from the finger tips [Fig. 21(b)(b')] leads to the formation of two vortices. Subsequently a jet is produced at each of the necking regions [Fig. 22(a)(a')] and the interfacial vorticity grows at the necking points until the minimum neck width is attained at $t \approx 2.28$.

3. $Re = 20000$

Finally, we end the series of computations for $We = 400$ with the case $Re = 20000$. The interfacial profile at representative times during the motion is shown in Fig. 23. Naturally, a faster interfacial motion is observed for this increased Reynolds number. The fingers are also thinner, show more deformation [Fig. 23(d)(e)(f)] than in the previous two cases, and an even more compact inner core during roll-up. The minimum width of the necking regions occurs at $t \approx 1.81$, Fig. 23(e), reaching a value of 5.1×10^{-3} or 10.46 L7 finest grid cells, but then the region gradually opens up as observed for the two smaller Reynolds numbers. Figure 24(a) provides a close-up of the L7 AMR mesh in the vicinity of one of the necking regions at $t = 1.81$ and the time history of the gap width is shown in Fig. 24(b). Note that the minimum neck width is about the same as that observed for $Re = 10000$. They differ by less that one quarter of a mesh cell. One would expect that as the Reynolds number increases the neck width would decrease as observed when going from $Re = 5000$ to $Re = 10000$. This could well be the case but unfortunately, even the L7 computations do not have the accuracy to resolve the difference between the $Re = 10000$ and $Re = 20000$ neck widths. What is clear however from Fig. 24 is that the interface is also escaping self-intersection for $Re = 20000$.

As observed for the previous cases viscosity produces an order one effect on the finger formation and subsequent roll-up. Figure 25(a) shows a comparison of the inviscid and viscous profiles at the inviscid collapse time. A comparison of the L6 and L7 resolutions for

the last computed time is given in Fig. 25(b) where one can see that except at the points of largest curvature, both interface profiles almost coincide within plotting resolution. Finally, the vorticity dynamics is depicted in Fig. 26 and Fig. 27. Larger values of interfacial vorticity are found and the pair of vortices at the bulk fluid are stronger that those for the smaller Reynolds numbers. There are also significant amounts of vorticity shed off the interface at late times during the motion as seen in Fig. 27(b)(c). This shed vorticity leads to an increased deformation of the interface.

The dynamics of the three $We = 400$ cases we have considered are qualitatively similar and as far as the computations show, there is no indication that finite-time pinching will happen for these initial conditions at a finite Reynolds number.

E. $We = 50$

We consider finally the case of an intermediate value of the Weber number, $We = 50$, for which a contrasting type of motion is expected based on the inviscid sheet computations reported by HLS[12]. Indeed, as HLS[12] demonstrated, for $We = 50$ and the same initial data we consider here, the vortex sheet does not roll-up. Instead the inviscid interface develops interpenetrating fingers that grow monotonically in time. As the fingers grow they also thin but there is no indication that a finite time interfacial collision will occur for this particular We and initial data.

We now look at the effects of viscosity in this motion for $Re = 20000$. Figure 28 shows the evolution of the sheared interface for $Re = 20000$ (left column) and contrasts it with that of the corresponding inviscid vortex sheet (right column). Already at $t = 3.0$, Fig. 28(a), we can see a difference in the shape of the fingers. The viscous fingers have a more curved tip, are slightly bulged at the center, and are wider than the inviscid ones. An incipient "necking" in the sheared interface is observed at $t = 4.0$, Fig. 28(b). Instead of continuing their lengthening in essentially the same inclined direction as in the inviscid case, the viscous fingers bend upwards [Fig. 28(c)]. The lengthening then ceases shortly after $t = 5.0$ and the viscous fingers begin to retract. An examination of the vorticity can help to understand the significant difference between the inviscid and viscous motions. Positive vorticity shed from the finger tips is transported and diffused both into the interior and the exterior of the fingers. The vorticity in the interior forms two round vortices as Fig. 29(a) shows. These

positive vortices tear off some of the negative interfacial vorticity at the necking points. The combined vorticity inside the necking regions increases the flux of fluid into the finger tips on one side of the neck and decreases it on the opposite side. This leads to an asymmetry in the finger tips and contributes to the bending of the fingers. As vorticity continues to be shed from the leading edges of the interface, Fig. 29(c), the K-H weakens and surface tension is able to stop the finger growth. The dynamic behavior up to this point is in accordance with the results reported by Tauber, Unverdi, and Tryggvason[13] for different data.

Figure 30 presents the subsequent evolution of the viscous interface as the fingers recede. The corresponding vorticity field and the scaled interfacial vorticity are plotted in Fig. 31. This longer time dynamics is striking. The sheared interface forms large pockets of fluid that, as the interface contracts, develop thin necks [Fig.30(b)]. As in $We = 400$, the necks reach a minimum value, here at $t \approx 7.1$, after which the disparate interface segments of the neck begin to separate. As this occurs, a point of high curvature begins to ensue at $x \approx 0.6$ and the periodically extended interface appears to collapse at this point [Fig. 30(c)]. The plots of vorticity in Fig. 31 contrast clearly two important events: first the formation of a jet in each of the necking regions [Fig. 31(b)] but with insufficient strength to drain all the fluid and overcome the viscous layer and second the large growth and concentration of interfacial vorticity [Fig. 31(c')] and a much stronger jet as the interface is about to collapse. Note that a different vertical scale was used to plot the interfacial vorticity in Fig. 31(c). The magnitude of the scaled interfacial vorticity at $t = 7.3$ exceeds for the first time in all our computations 0.5, the initial uniform value.

Close-ups of the L7 AMR mesh around the two contrasting regions are given in Fig. 32. The time history of the neck width is provided in Fig. 33(a) while Fig. 33(b) compares the behavior of the neck width (labeled one-period gap) and the collapsing gap width (labeled periodic extension gap) for $6.5 \leq t \leq 7.3$ measured in finest grid mesh cells. At $t = 7.3$, the collapsing gap has decreased to slightly less than 4 mesh points. L7 resolution cannot resolve any further decrease and thus the L7 computations for $t > 7.3$ would be unphysical. Nevertheless, the indications that the motion is going to be shortly terminated by the collapse of the interfaces are strong. A similar collapsing event was observed by HLS[12] for the inviscid vortex sheet at $We = 62.5$. We should note that there is an appreciable difference between the L6 and L7 time history curves in Fig. 33(a). The two curves share similar shapes but there appears to be a time-shift. As argued by Tauber, Unverdi, and Tryggvason[13], this is

likely to be the result of using a diffused interface approach as we do here. The spreading of surface tension forces becomes particularly important when the K-H weakens and the interface is pulled back. Since the surface tension forces are spread out more on the coarser L6 mesh the effect of surface tension is somewhat weaker. This results in a slightly slower motion than that observed for L7. The comparison of the L6 and L7 interface profiles given in Fig. 34 and the time history curves are consistent with this argument.

VI. DISCUSSION AND CONCLUDING REMARKS

So far as can be discerned from the $We = 50$, $Re = 20000$ numerics, a topological singularity can occur in a finite-viscosity 2D interfacial flow. HLS[12] identified the development of thin jets as being perhaps the basic structure in the formation of a topological singularity for the 2D inviscid vortex sheet motion. As seen in our numerical experiments the production and accumulation of vorticity has to be sustained at the narrow jets to make reconnection of the sheared interface possible. Motivated by these observations we now look at the dynamics of an isolated jet between two disjoint interfaces. To this end, we consider two symmetric interfaces whose initial positions are given in parametric form by

$$\mathbf{X}_1(\alpha, 0) = (\alpha, \quad 0.09 + 0.01\cos(2\pi\alpha)), \tag{50}$$

$$\mathbf{X}_2(\alpha, 0) = (\alpha, -0.09 - 0.01\cos(2\pi\alpha)), \tag{51}$$

for $0 \leq \alpha \leq 1$ and with initial vorticity distribution given by

$$w_0(x, y) = -\delta_h(\phi_1(x, y)) + \delta_h(\phi_2(x, y)), \tag{52}$$

where

$$\phi_1(x, y) = y - (0.09 + 0.01\cos(2\pi x))), \tag{53}$$

$$\phi_2(x, y) = y + (0.09 + 0.01\cos(2\pi x))). \tag{54}$$

We take $We = 50$ and $Re = 20000$. Figure 35(a) shows the jet at $t = 0$ and at $t = 1.1$, a time close to pinching. This picture also provides a resolution comparison of the L6 and L7 interface profiles. The profiles are indistinguishable within plotting resolution. The L7 AMR mesh is displayed in Fig. 35(b).

Figure 37 presents a time history of the inter-sheet distance for both the L6 and the L7 resolutions. At the last computed time, $t = 1.1$, the distance is $5.15 \times h_{\text{finest}} = 5.03 \times 10^{-3}$ and $4.94 \times h_{\text{finest}} = 2.41 \times 10^{-3}$ for L6 and L7 respectively with a clear indication of finite-time collapse. As Fig. 36 shows there is a strong concentration of vorticity at the collapsing region. At $t = 1.1$ the scaled interfacial vorticity at the necking points is greater than 0.8, even larger than the maximum value observed for the previous $We = 50$ pinching case.

The numerical evidence presented here shows that on one hand small but finite viscosity can remove the inviscid topological singularity in a rolled-up interface and on the other it provides strong support to the hypothesis that topological singularities can still happen for some intermediate We. There are several questions still unresolved; for example the structure of this singularity and the conditions under which it can occur in a 2D interfacial flow need to be better understood. We hope that our findings can stimulate more research in this direction.

Acknowledgments

We thank Marsha Berger, Lisa Fauci, Thomas Hou, Robert Krasny, John Lowenbrub, and Michael Shelley for insightful conversations and helpful comments. We are also very grateful to Fuz Rogers for his expert assistance with the computer systems to make possible the most intensive computations of this work. A.M.R. thanks the hospitality and support of the Department of Mathematics at UCSB which he visited for three months and during which some of the work was conducted. He is also grateful to the Department of Applied Math at the University of Sao Paulo for providing the conditions for this visit. H.D.C. acknowledges partial support by the National Science Foundation under Award Numbers DMS-0112388 and DMS-0311911, by the Faculty Career Development Award grant and the Academic Senate Junior Faculty Award grant. A.M.R. received partial financial support from FAPESP, grant # 00/02801-0, Brazil.

APPENDIX A: THE ALGORITHM

The computational scheme is a formally second order, pressure increment projection method. The core of the time discretization is the predictor-corrector scheme (17)–(29),

which as shown in Appendix B can be written as a more general iteration method. With that in mind, we summarize next the algorithm for the fully adaptive non-stiff method.

To obtain ($\mathbf{u}^{n+1}$, $\mathbf{X}^{n+1}$) from the previous time step known values ($\mathbf{u}^n$, $\mathbf{X}^n$), proceed as follows:

1. Advance wall-anchor points using (7).

   Consider the *initial guesses*

$$\begin{aligned} \mathbf{u}^{n+1,0} &= \mathbf{u}^n, \\ p^{n+\frac{1}{2},0} &= \begin{cases} 0 & \text{if } n = 0, \\ p^{n-\frac{1}{2}} & \text{if } n \geq 1, \end{cases} \\ \mathbf{X}^{n+1,0} &= \mathbf{X}^n . \end{aligned}$$

2. For the iteration index m varying from 1 to 2 do:

   - Spread forces from the Lagrangian to the Eulerian mesh

$$\mathbf{f}^{n+1,m-1} = \Delta\alpha \sum_{\mathrm{I}\cup\mathrm{W}} \mathbf{F}_k^{n+1,m-1} \delta_h(\mathbf{x} - \mathbf{X}_k^{n+1,m-1}) ,$$

     where $\mathbf{F}_k^{n+1,m-1}$ is given by

$$\mathbf{F}_k^{n+1,m-1} = \begin{cases} \tau \mathrm{D}_{\Delta\alpha} \left(\| \mathrm{D}_{\Delta\alpha} \mathbf{X}_k^{n+1,m-1} \|^{-1} \mathrm{D}_{\Delta\alpha} \mathbf{X}_k^{n+1,m-1} \right) & \text{for } k \in I, \\ -S_k \left(\mathbf{X}_k^{n+1,m-1} - \mathbf{X}_{\mathrm{W},k}^{n+1} \right) & \text{for } k \in W, \end{cases}$$

     and $\mathrm{D}_{\Delta\alpha}$ is the centered difference operator in α, i.e.,

$$\mathrm{D}_{\Delta\alpha} \mathbf{X}_k = (\mathbf{X}_{k+1} - \mathbf{X}_{k-1})/(2\Delta\alpha).$$

   - Compute the nonlinear and the singular terms at half time levels, by the averages

$$\begin{aligned} [(\mathbf{u}\cdot\nabla)\mathbf{u}]^{n+\frac{1}{2},m-1} &= \frac{1}{2}\{ [(\mathbf{u}\cdot\nabla)\mathbf{u}]^{n+1,m-1} + [(\mathbf{u}\cdot\nabla)\mathbf{u}]^n \}, \\ \mathbf{f}^{n+\frac{1}{2},m-1} &= \frac{1}{2}(\mathbf{f}^{n+1,m-1} + \mathbf{f}^n) . \end{aligned}$$

   - Solve for the provisional velocity field $\mathbf{u}^{*,m}$ (*projection parabolic step*)

$$\frac{\mathbf{u}^{*,m} - \mathbf{u}^n}{\Delta t} + \frac{\mathbf{G}\, p^{n+\frac{1}{2},m-1}}{\rho} = \frac{\mu}{\rho} L \left(\frac{\mathbf{u}^{*,m} + \mathbf{u}^n}{2}\right) - [(\mathbf{u}\cdot\nabla)\mathbf{u}]^{n+\frac{1}{2},m-1} + \frac{\mathbf{f}^{n+\frac{1}{2},m-1}}{\rho}$$

- Solve for the pressure $p^{n+\frac{1}{2},m}$, and for the velocity $\mathbf{u}^{n+1,m}$ (*projection elliptic step*) using $\mathbf{u}^{*,m}$:

$$\begin{aligned} \frac{\mathbf{u}^{n+1,m} - \mathbf{u}^n}{\Delta t} + \frac{\mathbf{G}\, p^{n+\frac{1}{2},m}}{\rho} &= \frac{\mathbf{u}^{*,m} - \mathbf{u}^n}{\Delta t} + \frac{\mathbf{G}\, p^{n+\frac{1}{2},m-1}}{\rho} \\ \mathbf{D} \cdot \mathbf{u}^{n+1,m} &= 0\,. \end{aligned}$$

- With the new Eulerian velocity field $\mathbf{u}^{n+1,m}$ update the immersed boundaries by

$$\begin{aligned} \frac{\mathbf{X}^{n+1,m} - \mathbf{X}^n}{\Delta t} = \frac{h^2}{2} \sum_{\mathbf{x}} \Big(\mathbf{u}^{n+1,m} \delta_h(\mathbf{x} - \mathbf{X}^{n+1,m-1}) + \mathbf{u}^n \delta_h(\mathbf{x} - \mathbf{X}^n) \Big) \\ + \frac{1}{2}(U_A^{n+1,m} \hat{\mathbf{t}}^{n+1,m-1} + U_A^n \hat{\mathbf{t}}^n)\,, \end{aligned}$$

  where, for the fluid interface, $U_A^{n+1,m}$ is computed from (16) using $\mathbf{u}^{n+1,m}$ and $\mathbf{X}^{n+1,m-1}$ and it is set to be identically zero for the markers on the walls.

- Apply the filtering procedure to wall points. If it is time, apply it also to fluid interface points.

3. Check whether or not it is time to remesh, changing to a new composite grid.

4. Update the clock, $t^{n+1} = t^n + \Delta t^n$, and select a new time step Δt^n based on the usual (first order) CFL stability condition.

This completes the algorithm.

APPENDIX B: GENERAL ITERATIVE SCHEME

It is interesting to note that if the *initial guesses*

$$\mathbf{u}^{n+1,0} = \mathbf{u}^n, \tag{B1}$$

$$p^{n+\frac{1}{2},0} = \begin{cases} 0 & \text{if } n = 0, \\ p^{n-\frac{1}{2}} & \text{if } n \geq 1, \end{cases} \tag{B2}$$

$$\mathbf{X}^{n+1,0} = \mathbf{X}^n\,. \tag{B3}$$

are considered, the predictor-corrector scheme (17)–(29) is just a particular case of the more general iteration

$$\frac{\mathbf{u}^{*,m}-\mathbf{u}^n}{\Delta t}+\frac{\mathbf{G}\,p}{\rho}^{n+\frac{1}{2},m-1}=\frac{\mu}{\rho}L\,(\frac{\mathbf{u}^{*,m}+\mathbf{u}^n}{2})-[(\mathbf{u}\cdot\nabla)\mathbf{u}]^{n+\frac{1}{2},m-1}+\frac{\mathbf{f}}{\rho}^{n+\frac{1}{2},m-1} \tag{B4}$$

$$\frac{\mathbf{u}^{n+1,m}-\mathbf{u}^n}{\Delta t}+\frac{\mathbf{G}\,p}{\rho}^{n+\frac{1}{2},m}=\frac{\mathbf{u}^{*,m}-\mathbf{u}^n}{\Delta t}+\frac{\mathbf{G}\,p}{\rho}^{n+\frac{1}{2},m-1} \tag{B5}$$

$$\mathbf{D}\cdot\mathbf{u}^{n+1,m}=0, \tag{B6}$$

$$\begin{aligned}\frac{\mathbf{X}^{n+1,m}-\mathbf{X}^n}{\Delta t}=\frac{h^2}{2}\sum_{\mathbf{x}}\Big(\mathbf{u}^{n+1,m}\delta_h(\mathbf{x}-\mathbf{X}^{n+1,m-1})\;+\;\mathbf{u}^n\delta_h(\mathbf{x}-\mathbf{X}^n)\Big)\,.\\ +\frac{1}{2}(U_A^{n+1,m}\hat{\mathbf{t}}^{n+1,m-1}+U_A^n\hat{\mathbf{t}}^n)\,,\end{aligned} \tag{B7}$$

with iteration index varying from 1 to 2.

The nonlinear and singular force terms, at half time levels, are given by the averages

$$[(\mathbf{u}\cdot\nabla)\mathbf{u}]^{n+\frac{1}{2},m-1}\;=\;\frac{1}{2}\{\,[(\mathbf{u}\cdot\nabla)\mathbf{u}]^{n+1,m-1}+[(\mathbf{u}\cdot\nabla)\mathbf{u}]^n\,\}, \tag{B8}$$

$$\mathbf{f}^{n+\frac{1}{2},m-1}\;=\;\frac{1}{2}(\,\mathbf{f}^{n+1,m-1}+\mathbf{f}^n\,)\,, \tag{B9}$$

where, for arbitrary indices n and m, one has

$$\mathbf{f}^{n+1,m-1}\;=\;\Delta s\sum_{k\in\,\mathrm{I}\cup\mathrm{W}}\mathbf{F}_k^{n+1,m-1}\delta_h(\mathbf{x}-\mathbf{X}_k^{n+1,m-1})\,. \tag{B10}$$

---

* Electronic address: `hdc@math.ucsb.edu`; URL: `http://www.math.ucsb.edu/~hdc`

† Electronic address: `roma@ime.usp.br`; URL: `http://www.ime.usp.br/~roma`

[1] P. Atsavapranee and M. Gharib. Structures in stratified plane mixing layers and the effects of cross-shear. *J. Fluid Mech.*, 342:53–86, 1997.

[2] D. W. Moore. The spontaneous appearance of a singularity in the shape of an evolving vortex sheet. *Proc. R. Soc. Lond. A*, 365:105–119, 1979.

[3] R. Caflisch and O. Orellana. Singular solutions and ill-posedness of the evolution of vortex sheets. *SIAM J. Math. Anal.*, 20:293–307, 1989.

[4] R. Krasny. A study of singularity formation in a vortex sheet by the point vortex approximation. *J. Fluid Mech.*, 167:65–93, 1986.

[5] D. I. Meiron, G. R. Baker, and S. A. Orszag. Analytic structure of vortex sheet dynamics. Part 1. Kelvin-Helmholtz instability. *J. Fluid Mech.*, 114:283–298, 1982.

[6] M. J. Shelley. A study of singularity formation in vortex sheet motion by a spectrally accurate vortex method. *J. Fluid Mech.*, 244:493–526, 1992.

[7] Q. Nie and G. R. Baker. Application of adaptive quadrature to axi-symmetric vortex-sheet motion. *J. Comput. Phys.*, 143:49–69, 1999.

[8] M. Nitsche. Singularity formation in a cylindrical and spherical vortex sheet. *J. Comput. Phys.*, 173:208–230, 2002.

[9] T. Sakajo. Formation of curvature singularity along vortex line in axisymmetric, swirling vortex sheet. *Phys. Fluids*, 14(8):2886–2896, 2002.

[10] S. Cowley, G. R. Baker, and S. Tanveer. On the formation of Moore curvature singularities in vortex sheet. *J. Fluid Mech.*, 378:233–267, 1999.

[11] T. Y. Hou, G. Hu, and P. Zhang. Singularity formation in 3-D vortex sheets. *Phys. Fluids*, 15(1):147–172, 2003.

[12] T. Y. Hou, J. S. Lowengrub, and M. J. Shelley. The long-time motion of vortex sheets with surface tension. *Phys. Fluids*, 9(7):1933–1954, 1997.

[13] W. Tauber, S. O. Unverdi, and G. Tryggvason. The nonlinear behavior of a sheared immiscible fluid interface. *Phys. Fluids*, 14(8):2871–2885, 2002.

[14] J. Glimm, J.W Grove, X.-L. Li, K. M Shyue, Y.N Zeng, and Q. Zhang. Three-dimensional front tracking. *SIAM J. Sci. Comput.*, 19(3):703–727, 1998.

[15] J. Glimm, J. Grove, X.-L. Li, and D. C. Tan. Robust computational algorithms for dynamic interface tracking in three dimensions. *SIAM J. Sci. Comput.*, 21(6):2240–2256, 2000.

[16] J. Glimm, J. W. Grove, X.L. Li, W. Oh, and D. H. Sharp. A critical analysis of Rayleigh-Taylor growth rates. *J. Comput. Phys.*, 169:652–677, 2001.

[17] Peskin, C.S. Numerical analysis of blood flow in the heart. *J. Comput. Phys.*, 25:220–252, 1977.

[18] S. O. Unverdi and G. Tryggvason. A front-tracking method for viscous, incompressible, multi-fluid flows. *J. Comput. Phys.*, 100:25–37, 1992.

[19] Mayo, A.A. & Peskin, C.S. An implicit numerical method for fluid dynamics problems with the immersed elastic boundaries. *Contemporary Mathematics*, 141:261–277, 1993.

[20] T. Y. Hou, J. S. Lowengrub, and M. J. Shelley. Removing the stiffness from interfacial flows with surface tension. *J. Comput. Phys.*, 114:312–338, 1994.

[21] J. M. Stockie and B. R. Wetton. Analysis of stiffness in the immersed boundary method and implications for time-stepping schemes. *J. Comput. Phys.*, 154:41–64, 1999.

[22] H. D. Ceniceros. The effect of surfactants on the formation and evolution of capillary waves. *Phys. Fluids*, 15(1):245–256, 2003.

[23] Roma, A.M.; Peskin, C.S.; Berger, M.J. An adaptive version of the immersed boundary method. *J. Comput. Phys.*, 153:509–534, 1999.

[24] Arthurs, K.M.; Moore, L.C.; Peskin, C.S.; Pitman, E.B. & Layton, H.E. Modeling arteriolar flow and mass transport using the immersed boundary method. *J. Comput. Phys.*, 147:402–440, 1998.

[25] G. Tryggvason, B. Bunner, A. Esmaeeli, D. Juric, N. Al-Rawahi, W. Tauber, J. Han, S. Nas, and Y.-J. Jan. A front-tracking method for computations of multiphase flow. *J. Comput. Phys.*, 169:708–759, 2001.

[26] M. S. Longuet-Higgins and E. D. Cokelet. The deformation of steep surface waves on water I. A numerical method of computation. *Proc. R. Soc. Lond. A.*, 350:1–26, 1976.

[27] R. Peyret and T.D Taylor. *Computational Methods for Fluid Flow.* Springer-Verlag, New York, 1990.

[28] Berger, M.J. & Colella, P. Local adaptive mesh refinement for shock hydrodynamics. *J. Comput. Phys.*, 82:64–84, 1989.

[29] Berger, M.J. & Rigoutsos, I. An algorithm for point clustering and grid generation. *IEEE Transactions on Systems, Man, and Cybernetics*, 21(5):1278–1286, September/October 1991.

[30] Roma, A.M. *A Multilevel Self-adaptive Version of the Immersed Boundary Method.* PhD thesis, Courant Institute of Mathematical Sciences – New York University, January 1996. University Microfilms # 9621828.

[31] Howell, L.H. A multilevel adaptive projection method for unsteady incompressible flow. Technical Report UCRL-JC-112327, Lawrence Livermore National Laboratory, Livermore, CA 94550, May 1993.

[32] Minion, M.L. A note on the stability of godunov projection methods. Technical Report 95-002, Courant Institute of Mathematical Sciences – New York University, January 1995.

[33] Minion, M.L. A projection method on locally refined grids. *J. Comput. Phys.*, 127(1):158–178, 1996.

[34] U.M. Ascher, S.J. Ruuth, and B. Wetton. Implicit-explicit methods for time-dependent pde's. *SIAM J Numer. Anal.*, 32:797, 1995.

[35] H. D. Ceniceros and T. Y. Hou. Convergence of a non-stiff boundary integral method for

interfacial flows with surface tension. *Math. Comput.*, 67:137–182, 1998.

[36] T. Funada and D. D. Joseph. Viscous potential flow analysis of Kelvin-Helmholtz instability in a channel. *J. Fluid Mech.*, 445:263–283, 2001.

LIST OF FIGURE CAPTIONS

Figure 1. Typical Eulerian and Lagrangian ("•") meshes.

Figure 2. Location of coarse and fine variables.

Figure 3. $We = 200$. Left column, $Re = 20000$, $L7$. Right column, inviscid sheet. (a) and (a') $t = 0.70$, (b) and (b') $t = 1.0$, (c) and (c') $t = 1.41$.

Figure 4. Vorticity: $We = 200$, $Re = 20000$, $L7$. (a) and (a') $t = 0.70$, (b) and (b') $t = 1.0$, (c) and (c') $t = 1.41$. Right column, flooded contour plot. Left column, scaled sheet vorticity $h_{\text{finest}} \times \omega$ versus the Lagragian marker α.

Figure 5. $We = 200$, $Re = 20000$, $L7$, longer time dynamics. (a) $t = 2.0$, (b) $t = 2.5$, (c) $t = 3.2$, and (d) $t = 3.8$.

Figure 6. Vorticity: $We = 200$, $Re = 20000$, $L7$. (a) and (a') $t = 2.0$, (b) and (b') $t = 2.5$. Right column, flooded contour plot. Left column, scaled sheet vorticity $h_{\text{finest}} \times \omega$ versus the Lagragian marker α.

Figure 7. Vorticity: $We = 200$, $Re = 20000$, $L7$. (c) and (c') $t = 3.2$, (d) and (d') $t = 3.8$. Right column, flooded contour plot. Left column, scaled sheet vorticity $h_{\text{finest}} \times \omega$ versus the Lagragian marker α.

Figure 8. $We = 200$, $Re = 20000$, $L7$, longer time dynamics. (a) $t = 4.23$ and (b) $t = 4.78$.

Figure 9. Vorticity: $We = 200$, $Re = 20000$, $L7$. (c) and (c') $t = 4.23$, (d) and (d') $t = 4.78$. Right column, flooded contour plot. Left column, scaled sheet vorticity $h_{\text{finest}} \times \omega$ versus the Lagragian marker α.

Figure 10. (a) Comparison of the $We = 200$, $Re = 20000$ interface profiles for L6 (dashed-dotted) and L7 (solid) resolutions. (a) $t = 4.0$ and (b) $t = 4.78$.

Figure 11. Time behavior of the smallest interfacial gap for L6 and L7 resolutions. $We = 200$, $Re = 20000$. The minimum is 10.75 and 26.6 finest grid points for L6 and L7, respectively.

Figure 12. Inviscid vortex sheet, $We = 400$. (a) $t = 0.50$, (b) $t = 0.60$, (c) $t = 0.70$, and (d) $t = 0.82$.

Figure 13. Viscous interface $Re = 5000$ and $We = 400$, L7. (a) $t = 0.7$, (b) $t = 1.0$, (c) $t = 1.6$, (d) $t = 2.3$, (e) $t = 3.07$, and (f) $t = 3.5$.

Figure 14. (a) $We = 400$ and $Re = 5000$. (a) Close-up of AMR mesh around the minimum width neck and (b) time history of the neck width.

Figure 15. (a) Comparison of the inviscid (solid) and the $Re = 5000$,$We = 400$ interface profile (dashed) at $t = 0.82$. (b) Resolution comparison for L6 and L7 at final time $t = 3.5$.

Figure 16. Vorticity: $We = 400$, $Re = 5000$, $L7$. (a) and (a') $t = 0.70$, (b) and (b') $t = 1.0$, (c) and (c') $t = 1.6$. Right column, flooded contour plot. Left column, scaled sheet vorticity $h_{\text{finest}} \times \omega$ versus the Lagragian marker α.

Figure 17. Vorticity: $We = 400$, $Re = 5000$, $L7$. (a) and (a') $t = 2.3$, (b) and (b') $t = 3.07$, (c) and (c') $t = 3.5$. Right column, flooded contour plot. Left column, scaled sheet vorticity $h_{\text{finest}} \times \omega$ versus the Lagragian marker α.

Figure 18. Viscous interface $Re = 10000$ and $We = 400$, L7. (a) $t = 0.7$, (b) $t = 1.0$, (c) $t = 1.6$, (d) $t = 1.8$, (e) $t = 2.28$, and (f) $t = 2.5$.

Figure 19. (a) $We = 400$ and $Re = 10000$. (a) Close-up of AMR mesh around the minimum width neck and (b) time history of the neck width.

Figure 20. (a) Comparison of the inviscid (solid) and the $Re = 10000$, $We = 400$ interface

profile (dashed) at $t = 0.82$. (b) Resolution comparison for L6 and L7 at final time $t = 2.5$.

Figure 21.Vorticity: $We = 400$, $Re = 10000$, $L7$. (a) and (a') $t = 0.70$, (b) and (b') $t = 1.0$, (c) and (c') $t = 1.6$. Right column, flooded contour plot. Left column, scaled sheet vorticity $h_{\text{finest}} \times \omega$ versus the Lagragian marker α.

Figure 22. Vorticity: $We = 400$, $Re = 10000$, $L7$. (a) and (a') $t = 1.8$, (b) and (b') $t = 2.28$, (c) and (c') $t = 2.5$. Right column, flooded contour plot. Left column, scaled sheet vorticity $h_{\text{finest}} \times \omega$ versus the Lagragian marker α.

Figure 23. Viscous interface $Re = 20000$ and $We = 400$, L7. (a) $t = 0.7$, (b) $t = 1.0$, (c) $t = 1.3$, (d) $t = 1.6$, (e) $t = 1.81$, and (f) $t = 2.24$.

Figure 24. (a) $We = 400$ and $Re = 20000$. (a) Close-up of AMR mesh around the minimum width neck and (b) time history of the neck width.

Figure 25. (a) Comparison of the inviscid (solid) and the $Re = 20000$, $We = 400$ interface profile (dashed) at $t = 0.82$. (b) Resolution comparison for L6 and L7 at final time $t = 2.24$.

Figure 26. Vorticity: $We = 400$, $Re = 20000$, $L7$. (a) and (a') $t = 0.70$, (b) and (b') $t = 1.0$, (c) and (c') $t = 1.3$. Right column, flooded contour plot. Left column, scaled sheet vorticity $h_{\text{finest}} \times \omega$ versus the Lagragian marker α.

Figure 27. Vorticity: $We = 400$, $Re = 20000$, $L7$. (a) and (a') $t = 1.6$, (b) and (b') $t = 1.81$, (c) and (c') $t = 2.24$. Right column, flooded contour plot. Left column, scaled sheet vorticity $h_{\text{finest}} \times \omega$ versus the Lagragian marker α.

Figure 28. $We = 50$. Left column, $Re = 20000$, $L7$. Right column, inviscid sheet. (a) and (a') $t = 3.0$, (b) and (b') $t = 4.0$, (c) and (c') $t = 5.0$.

Figure 29. Vorticity: $We = 50$, $Re = 20000$, $L7$. (a) and (a') $t = 3.0$, (b) and (b') $t = 4.0$, (c) and (c') $t = 5.0$. Right column, flooded contour plot. Left column, scaled sheet vorticity

$h_{\text{finest}} \times \omega$ versus the Lagragian marker α.

Figure 30. $We = 50$ and $Re = 20000$, $L7$. (a) $t = 6.5$, (b) $t = 7.1$, and (c) $t = 7.3$.

Figure 31. Vorticity: $We = 50$, $Re = 20000$, $L7$. (a) and (a') $t = 6.5$, (b) and (b') $t = 7.1$, (c) and (c') $t = 7.3$. Right column, flooded contour plot. Left column, scaled sheet vorticity $h_{\text{finest}} \times \omega$ versus the Lagragian marker α.

Figure 32. Close-ups of the regions with the smallest interfacial gaps. (a) $t = 7.1$ and $t = 7.3$.

Figure 33. $We = 50$ and $Re = 20000$. Time history of the minimum gap in (a) the one-period interface and (b) the periodically extended interface.

Figure 34. $We = 50$ and $Re = 20000$. Resolution comparison. L6 (dotted) and L7 (solid) at (a) $t = 6.0$ and (b) the time the minimum neck width is attained.

Figure 35. A pinching jet, $We = 50$ and $Re = 20000$. (a) $t = 0$ (dotted) and $t = 1.1$ (solid) for both L6 and L7 resolutions. (b) The AMR L7 composite grid and the sheets at $t = 1.1$.

Figure 36. Vorticity of the pinching jet at $t = 1.1$, $We = 50$ and $Re = 20000$, L7. (a) Flooded contour plot of the vorticity field near the pinching region and (b) scaled vorticity (ωh_{finest}) along the upper (solid) and the lower sheet (dashed).

Figure 37. Time behavior of the jet's inter-sheet distance for L6 (dashed) and L7 (solid).

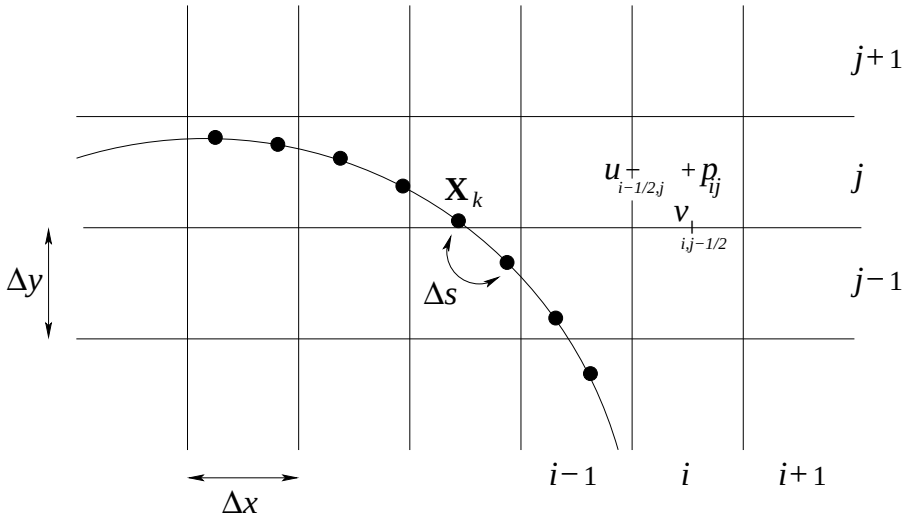

FIG. 1: Ceniceros and Roma, Physics of Fluids

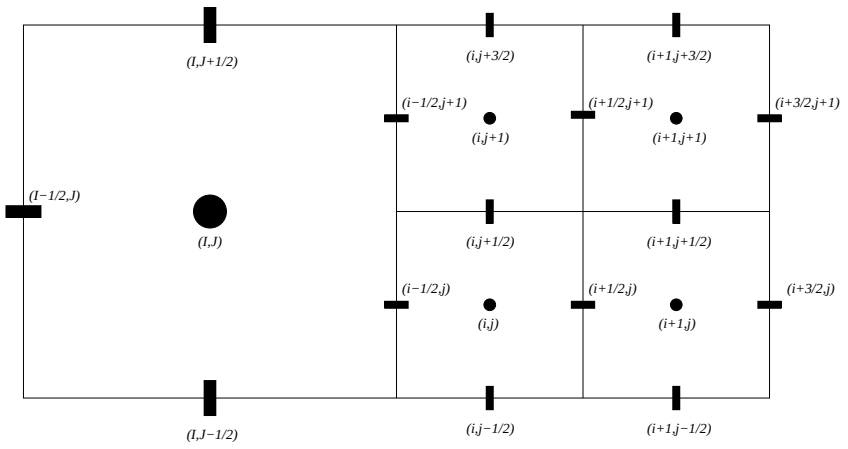

FIG. 2: Ceniceros and Roma, Physics of Fluids

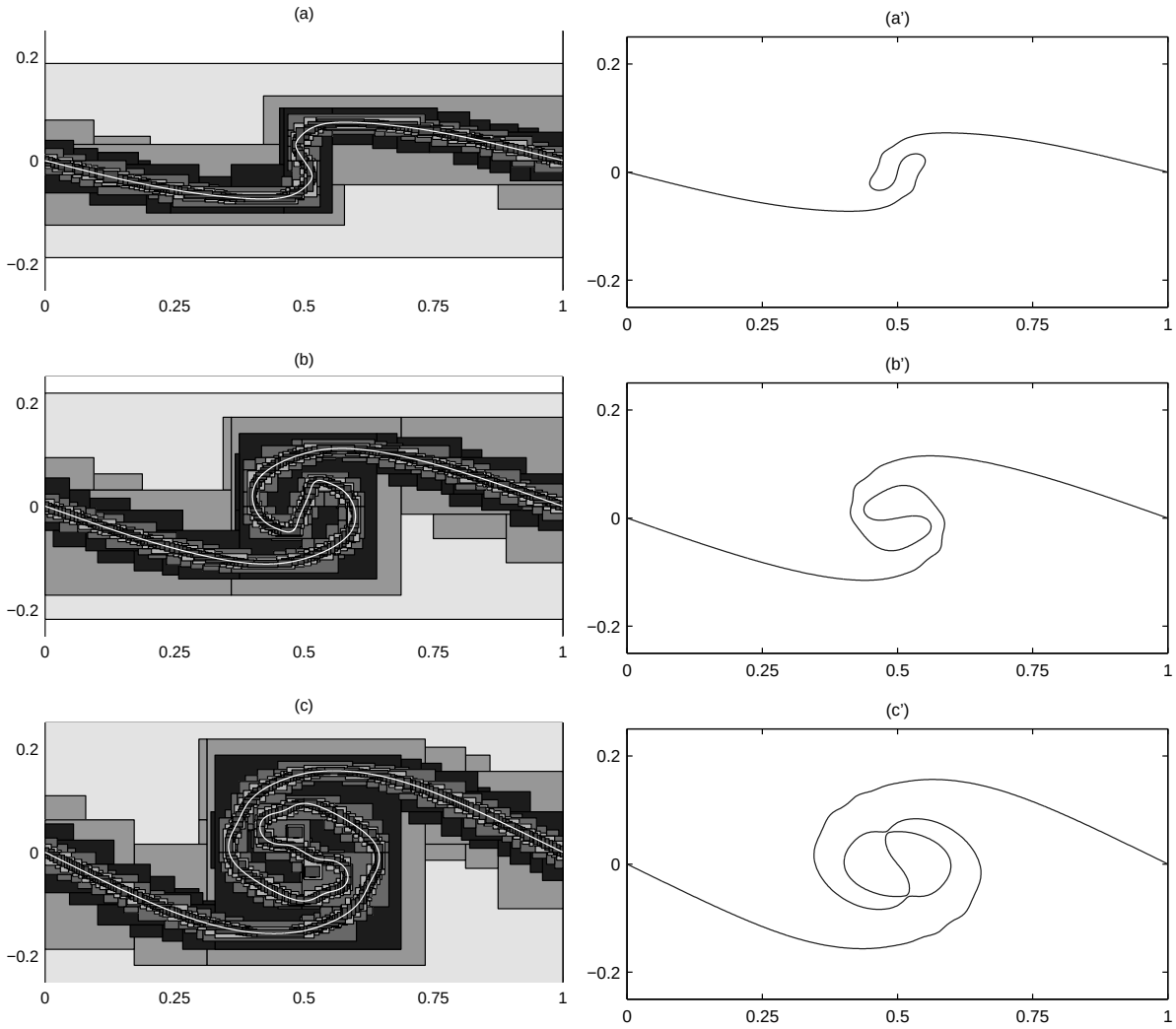

FIG. 3: Ceniceros and Roma, Physics of Fluids

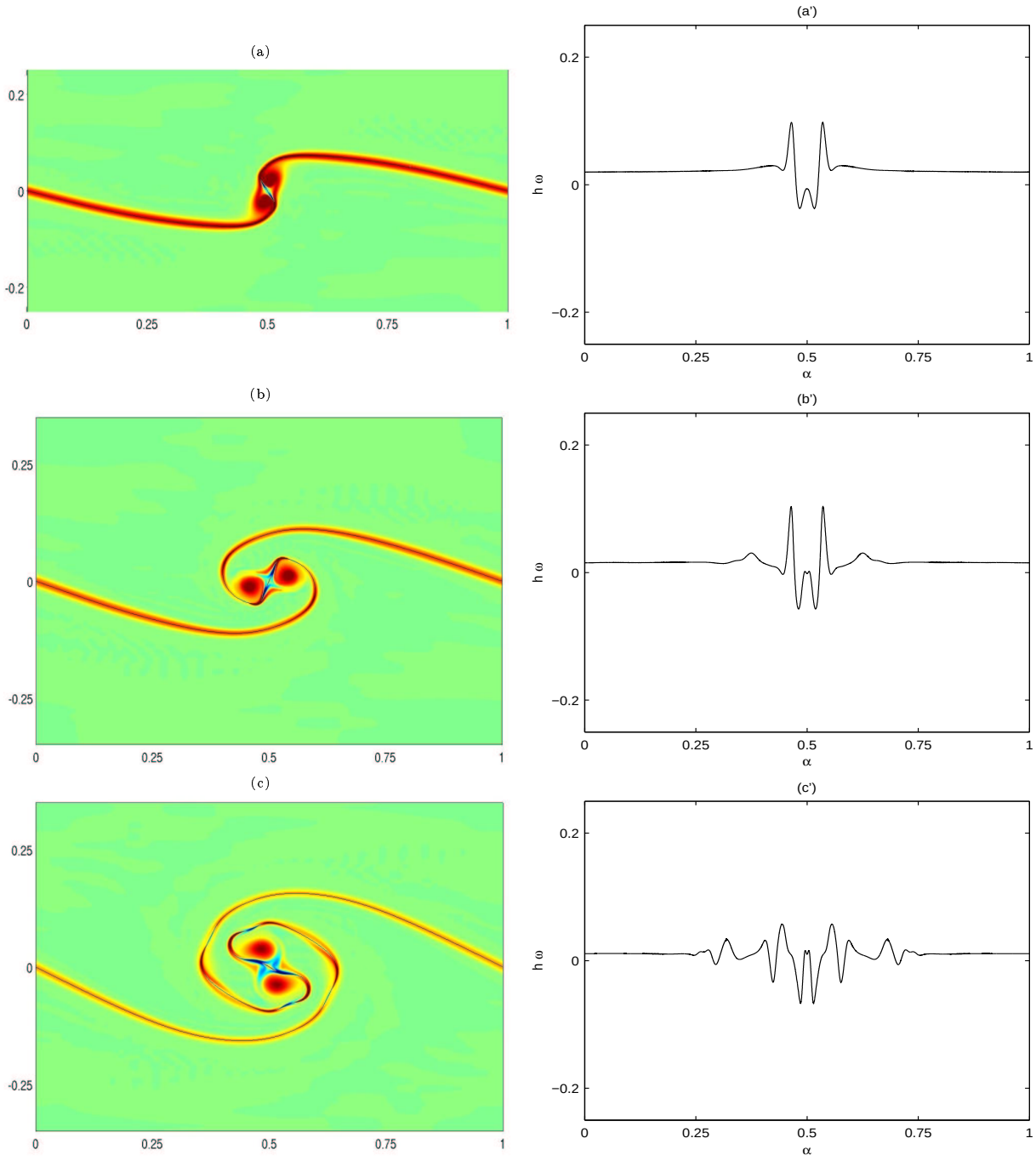

FIG. 4: Ceniceros and Roma, Physics of Fluids

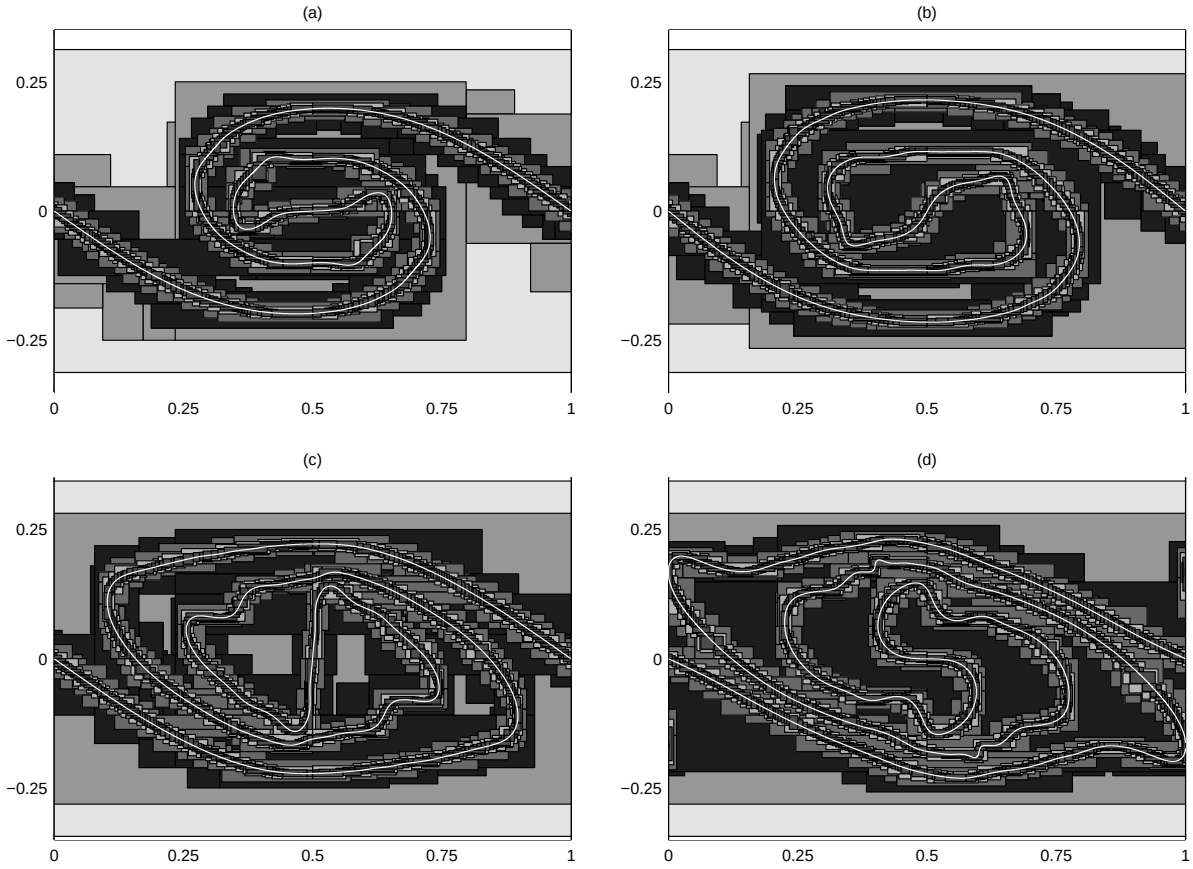

FIG. 5: Ceniceros and Roma, Physics of Fluids

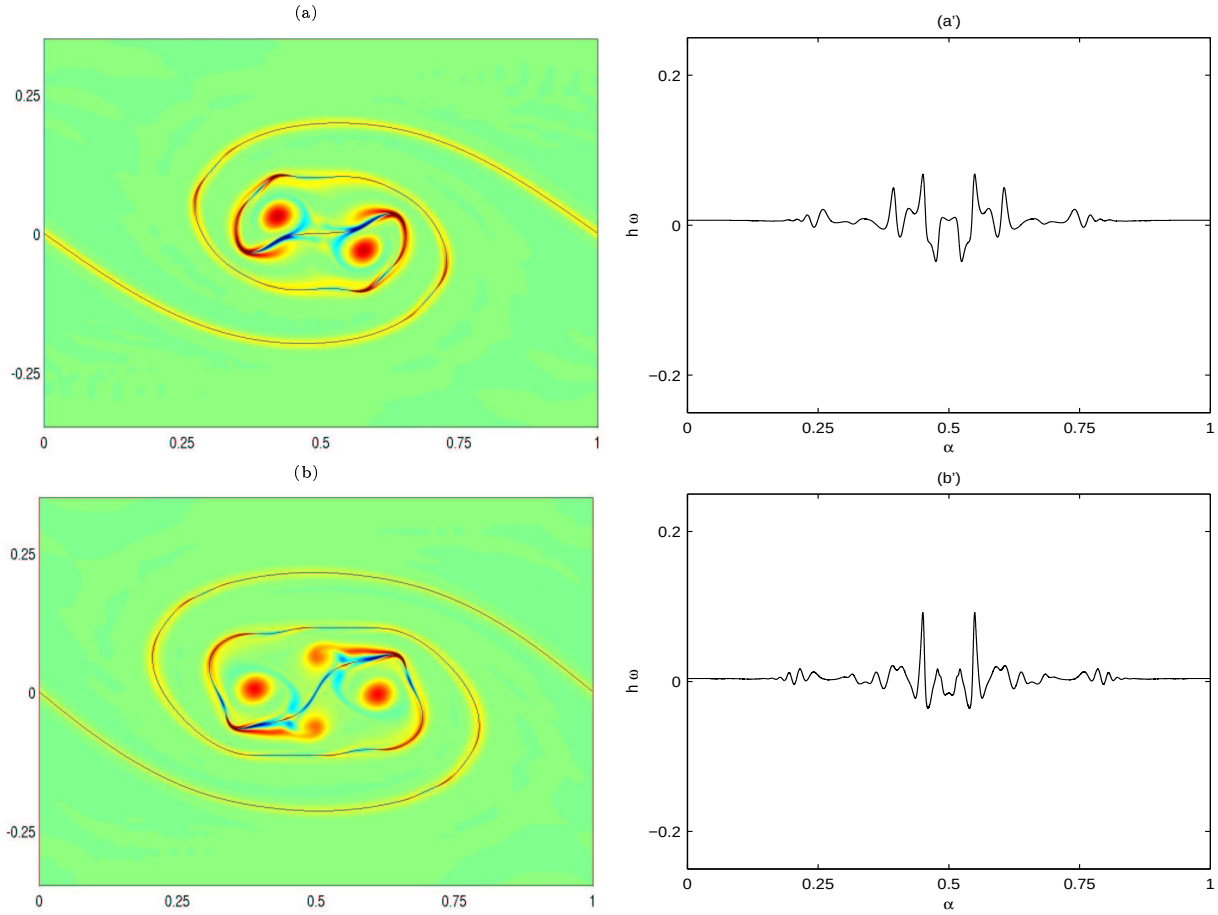

FIG. 6: Ceniceros and Roma, Physics of Fluids

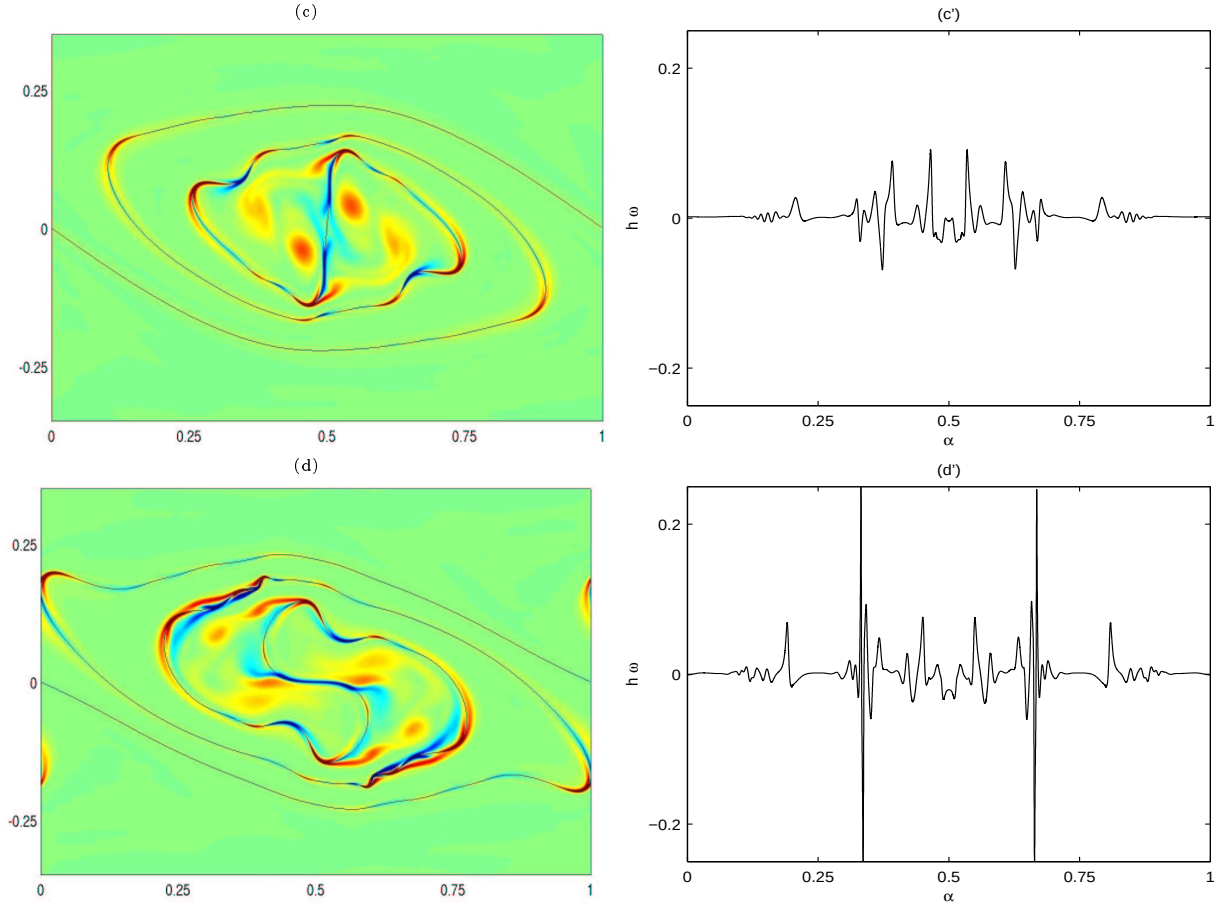

FIG. 7: Ceniceros and Roma, Physics of Fluids

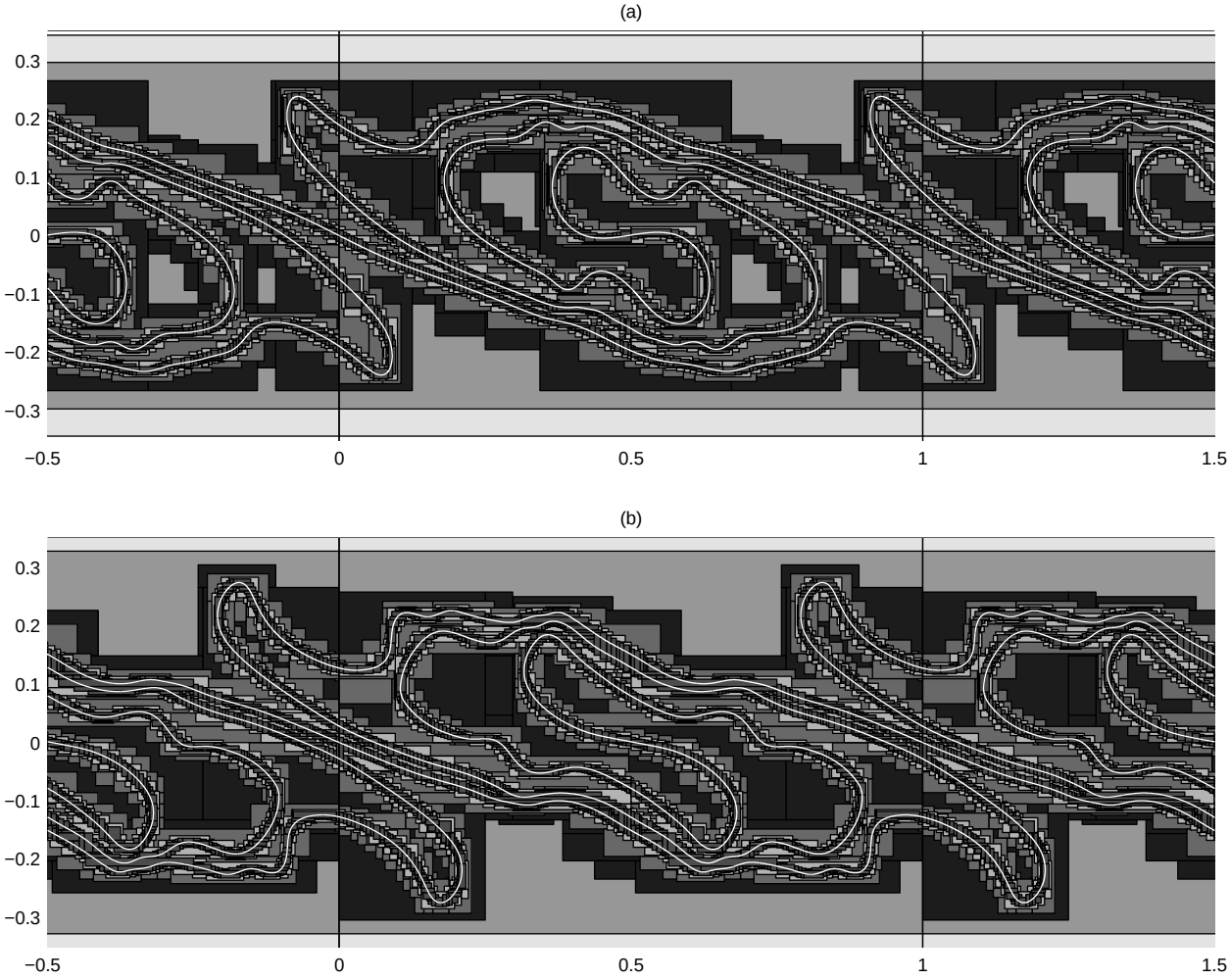

FIG. 8: Ceniceros and Roma, Physics of Fluids

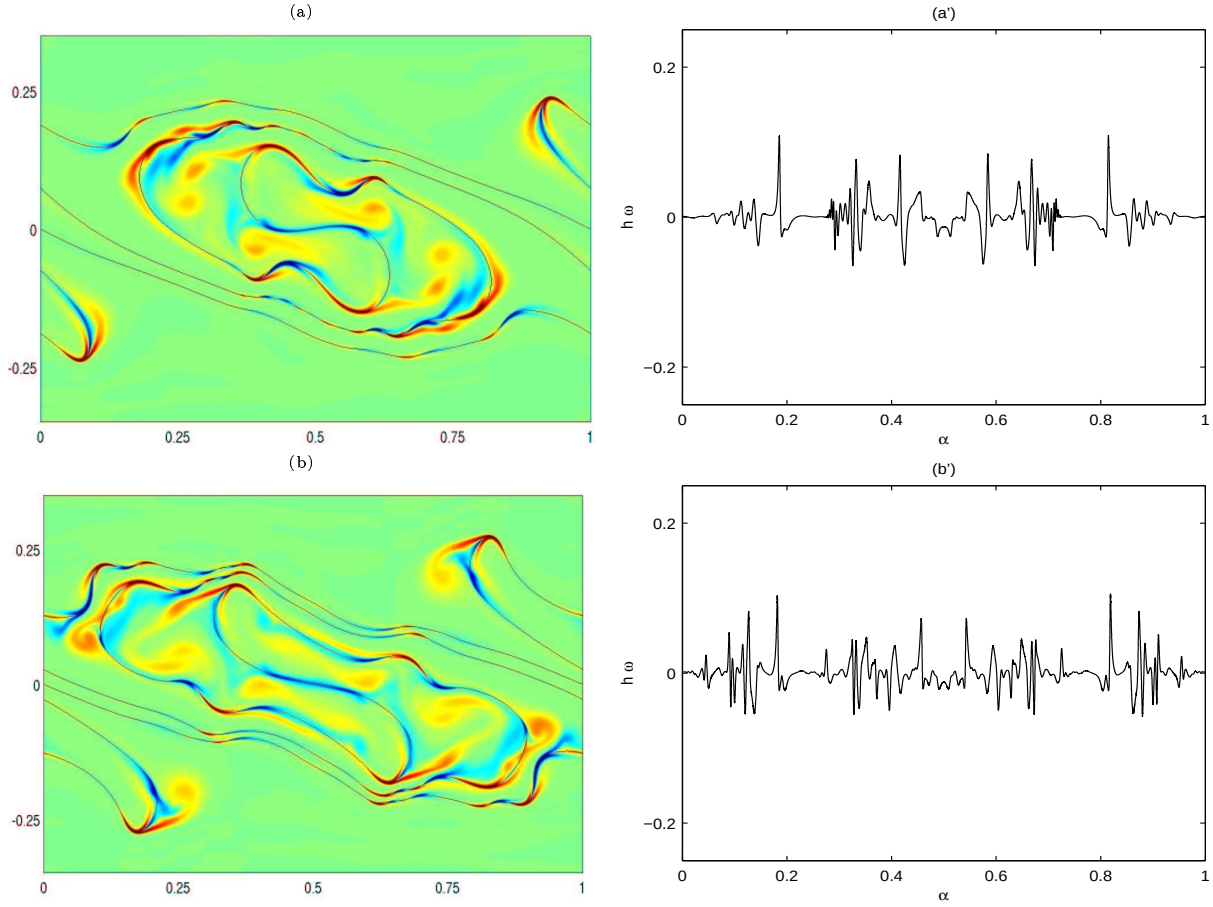

FIG. 9: Ceniceros and Roma, Physics of Fluids

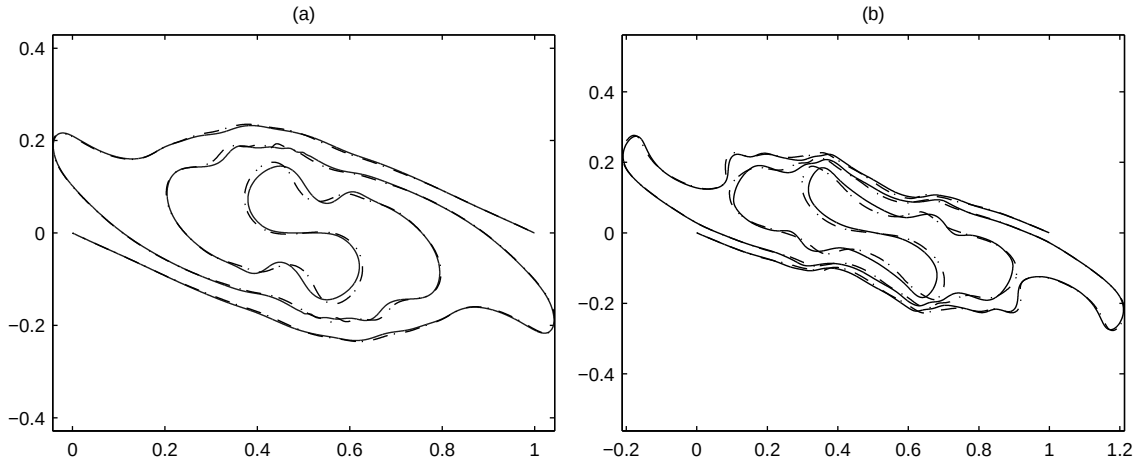

FIG. 10: Ceniceros and Roma, Physics of Fluids

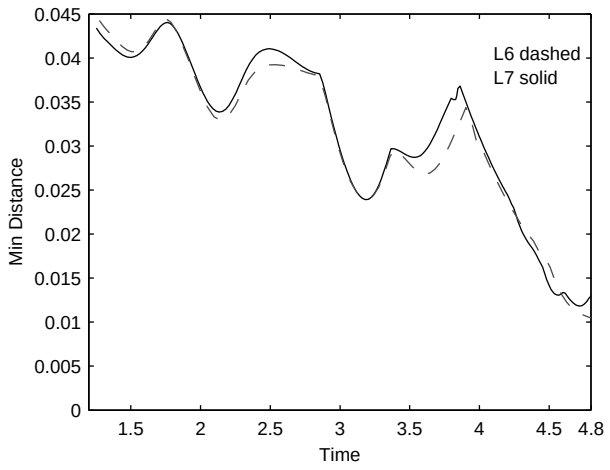

FIG. 11: Ceniceros and Roma, Physics of Fluids

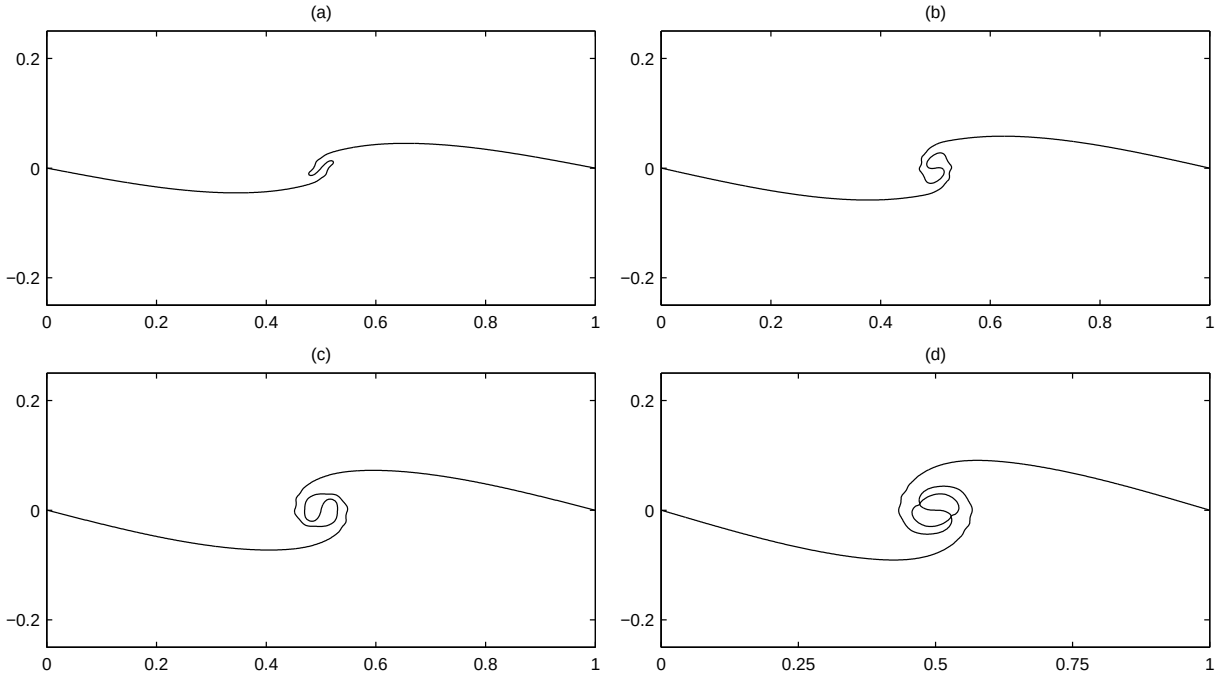

FIG. 12: Ceniceros and Roma, Physics of Fluids

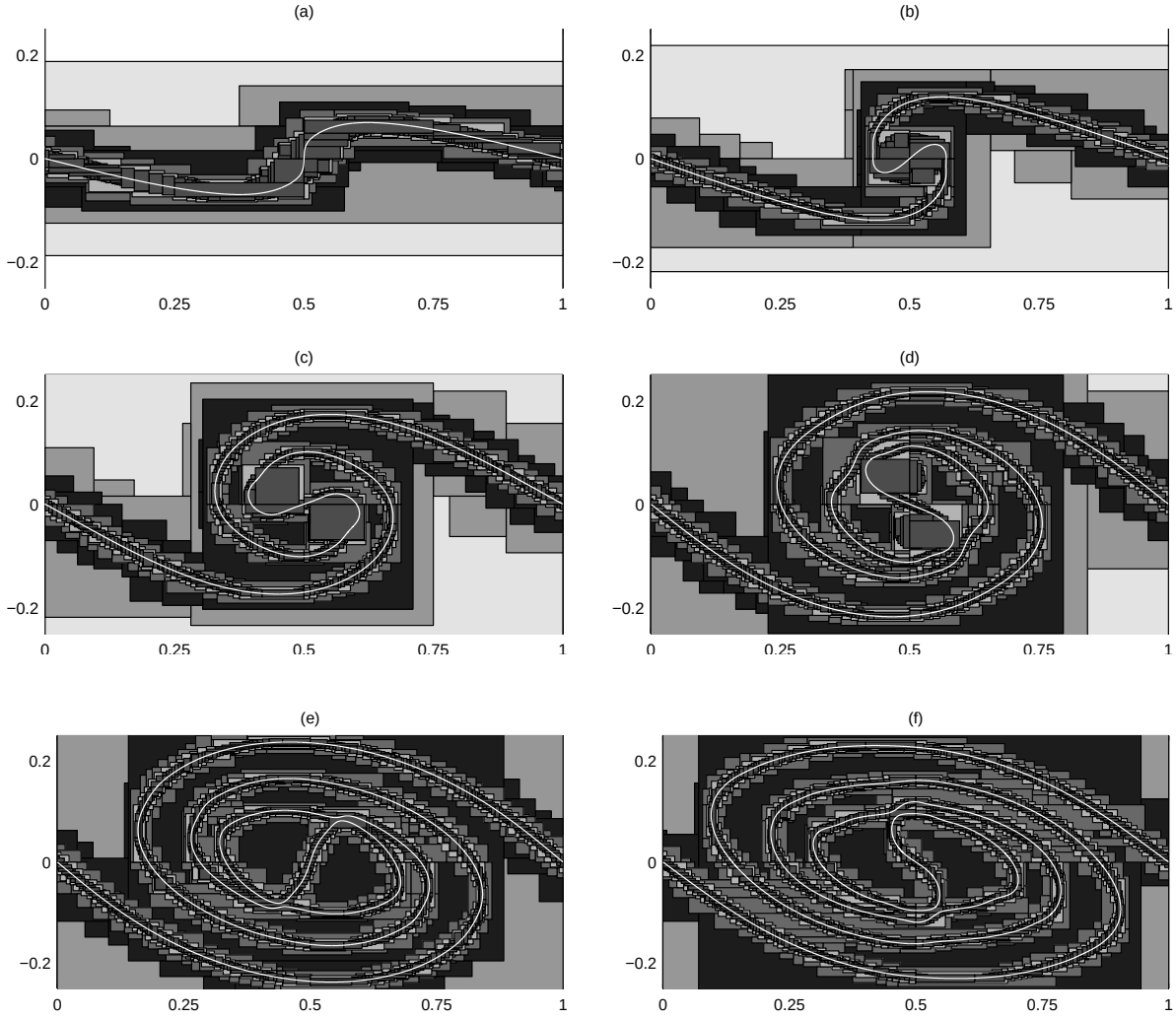

FIG. 13: Ceniceros and Roma, Physics of Fluids

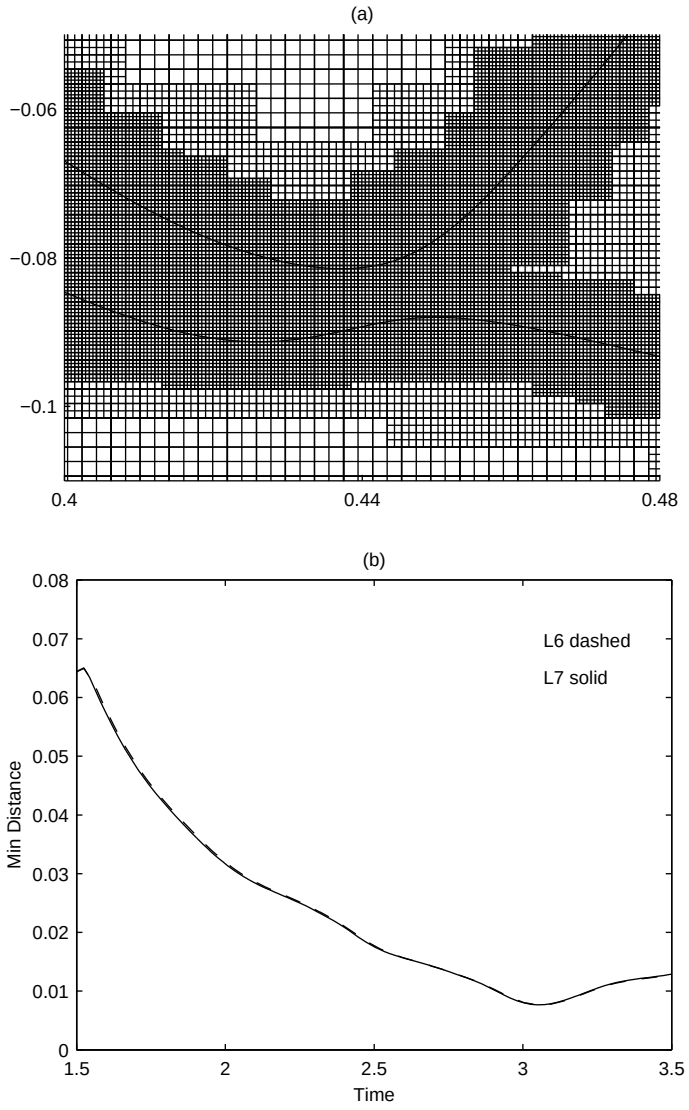

FIG. 14: Ceniceros and Roma, Physics of Fluids

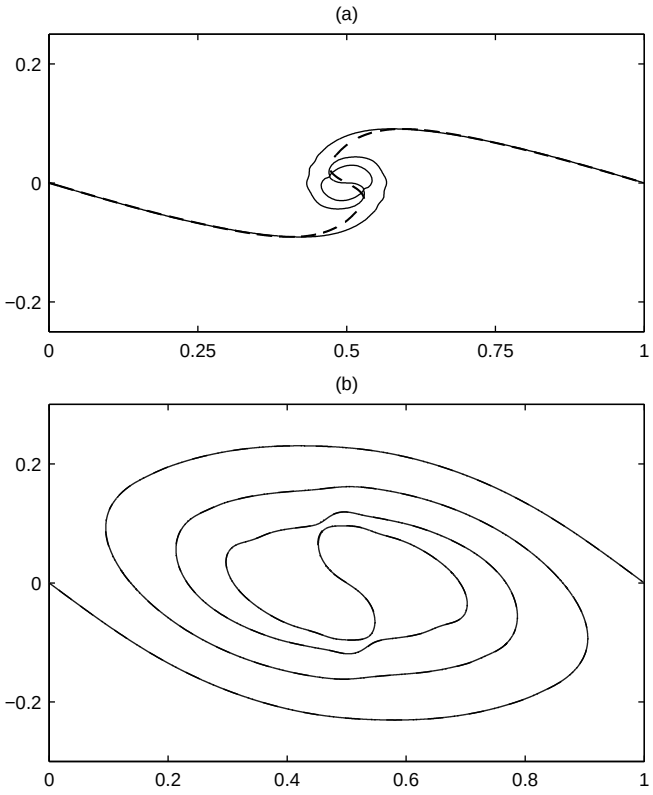

FIG. 15: Ceniceros and Roma, Physics of Fluids

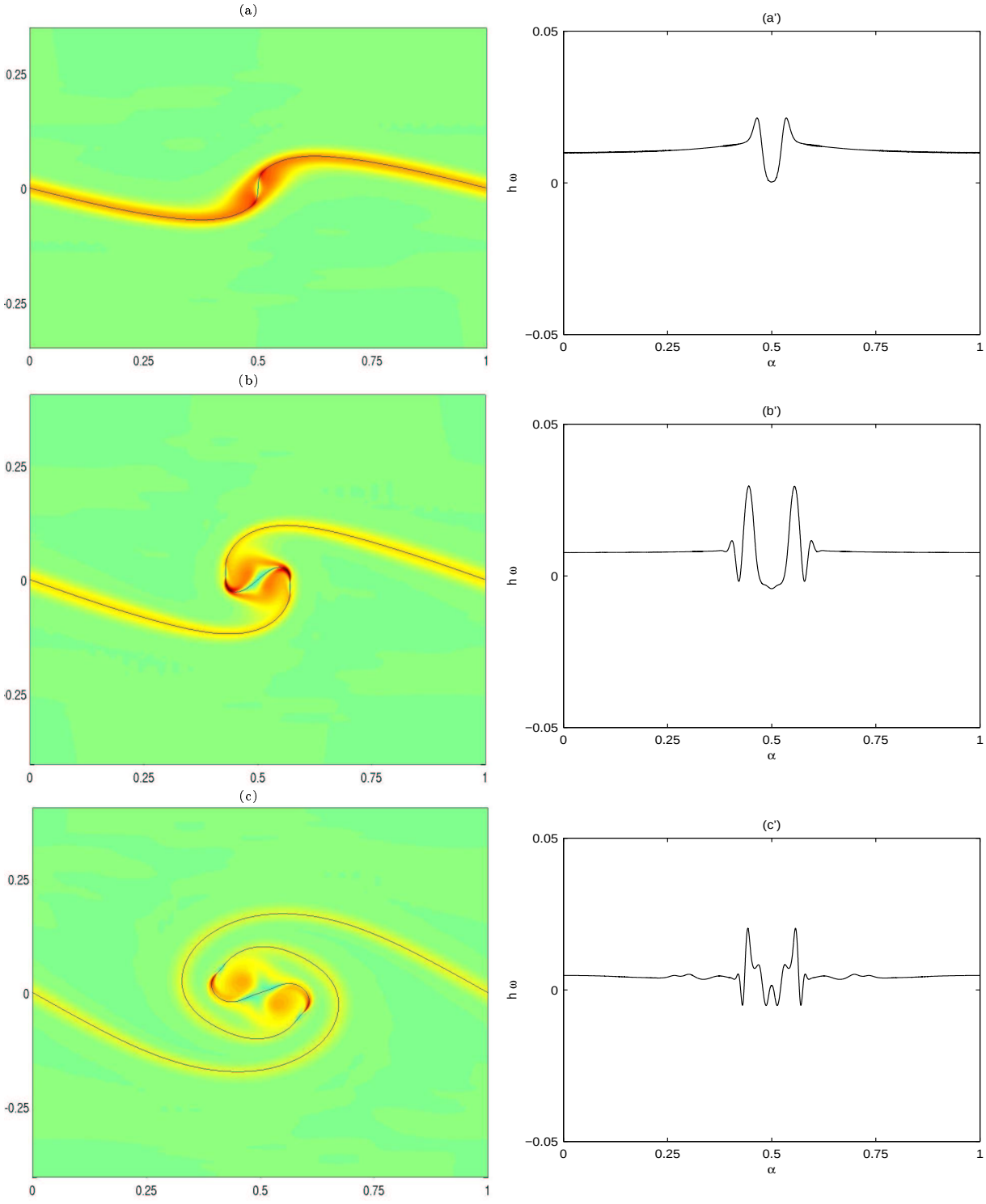

FIG. 16: Ceniceros and Roma, Physics of Fluids

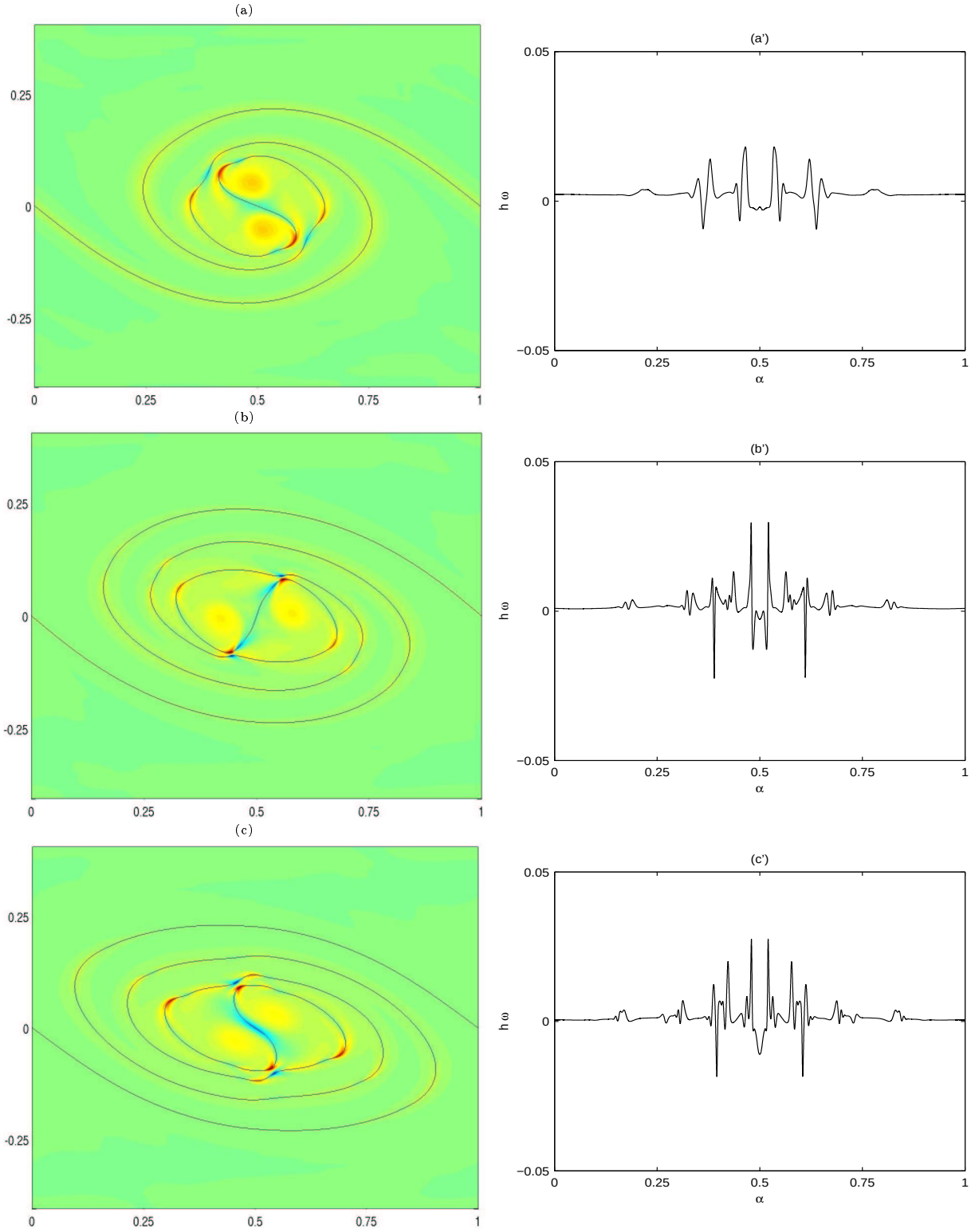

FIG. 17: Ceniceros and Roma, Physics of Fluids

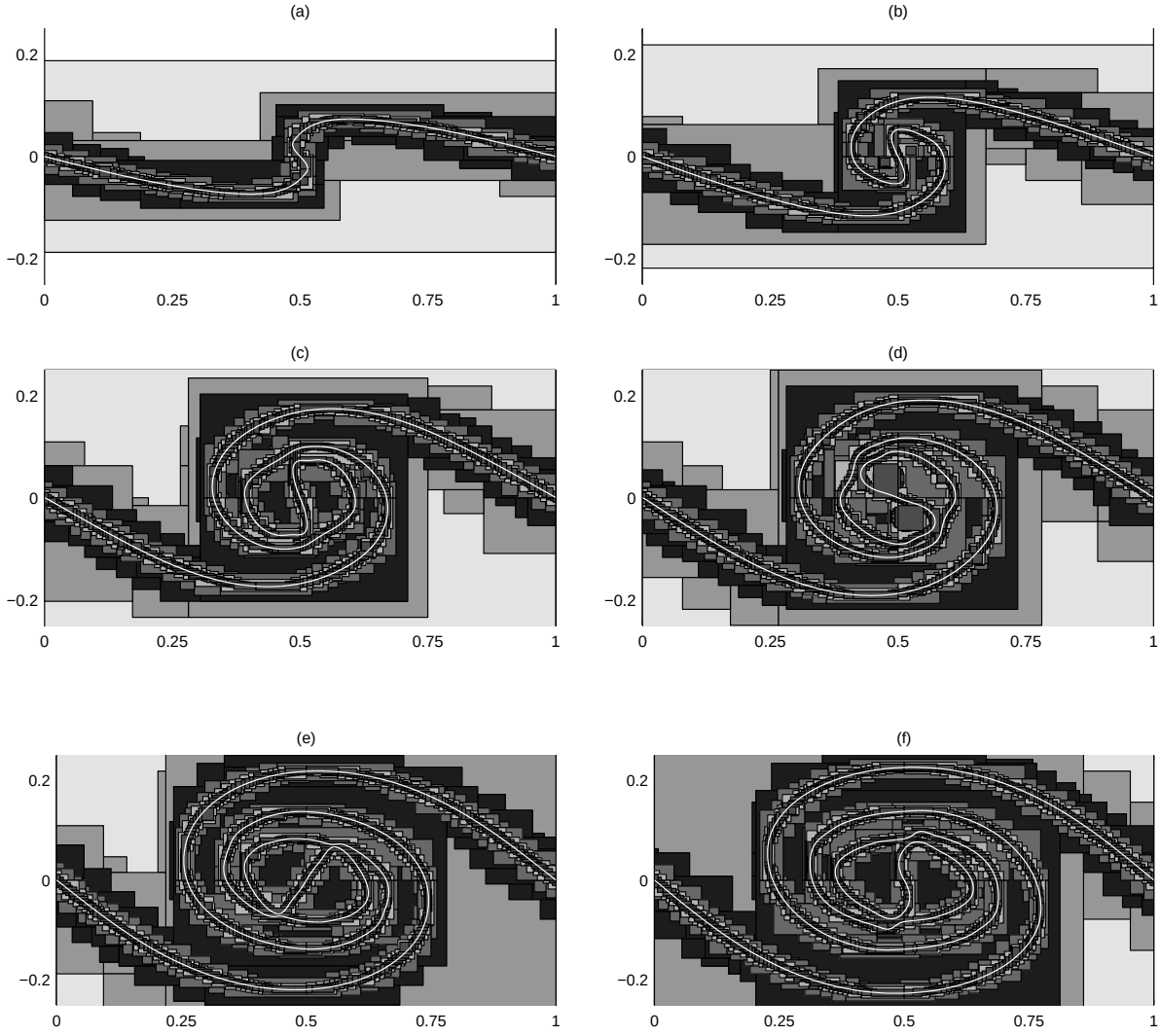

FIG. 18: Ceniceros and Roma, Physics of Fluids

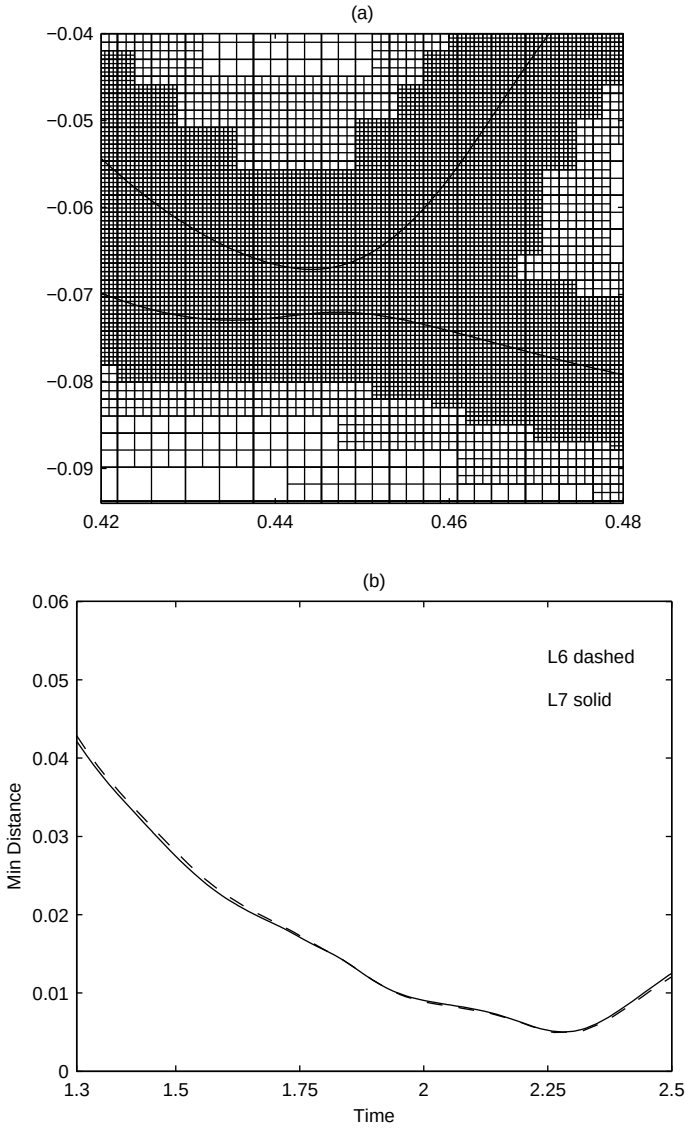

FIG. 19: Ceniceros and Roma, Physics of Fluids

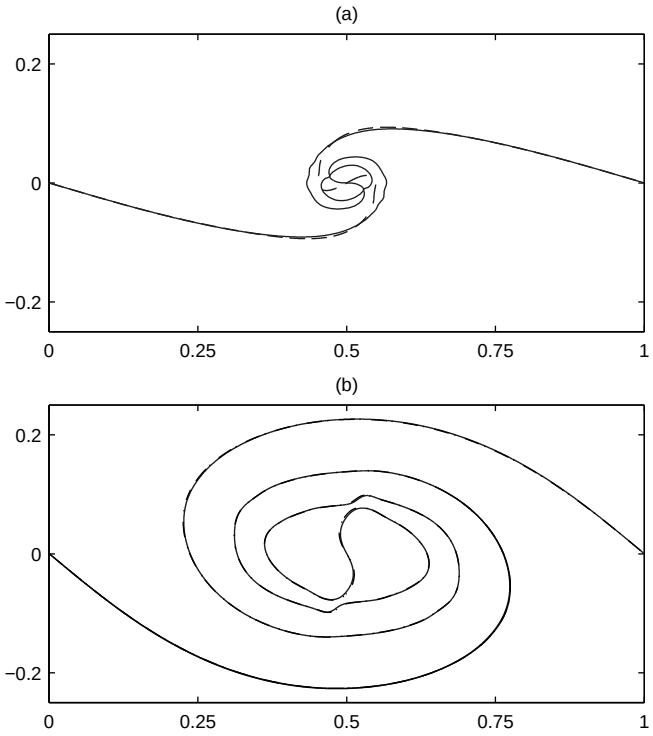

FIG. 20: Ceniceros and Roma, Physics of Fluids

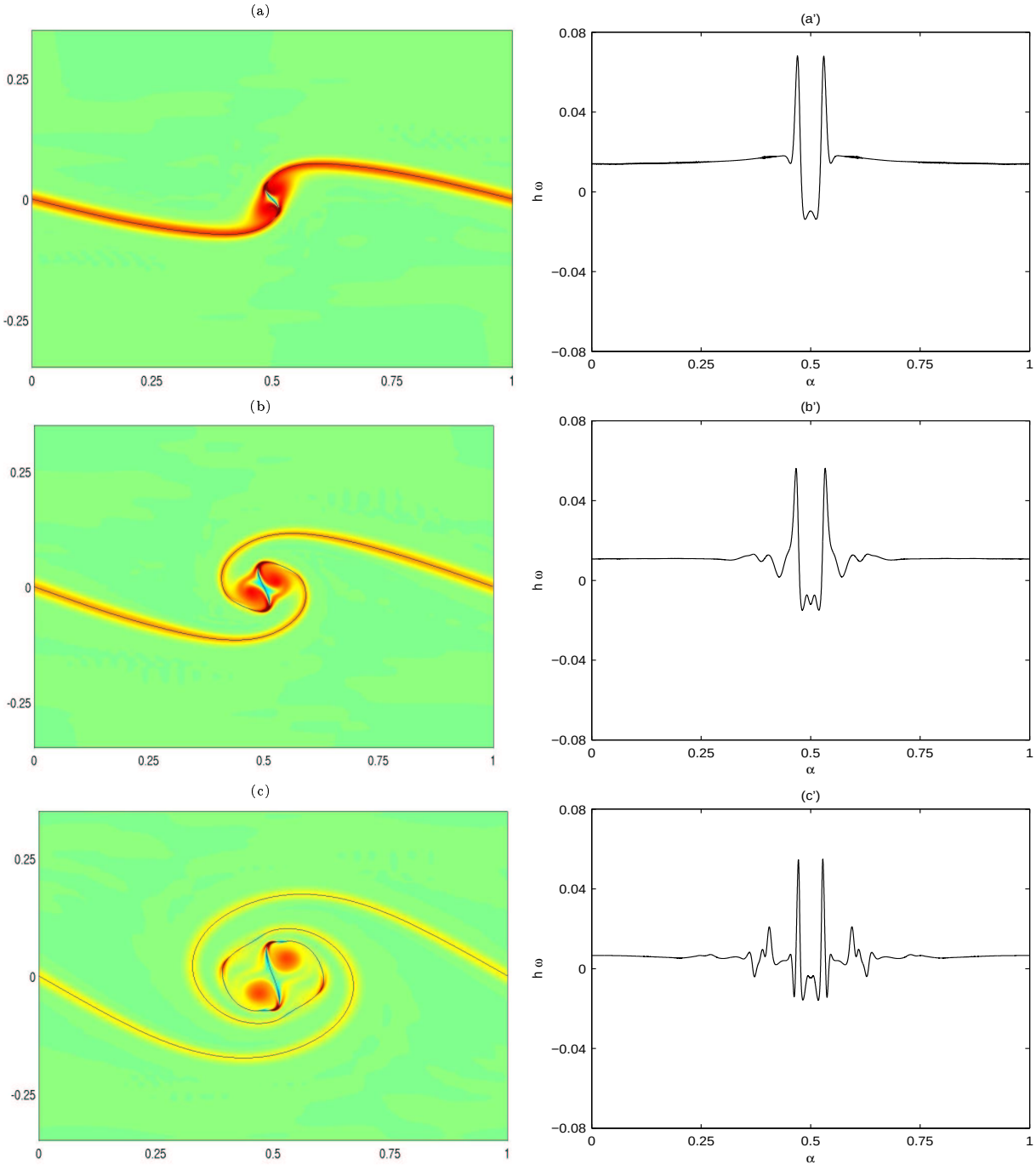

FIG. 21: Ceniceros and Roma, Physics of Fluids

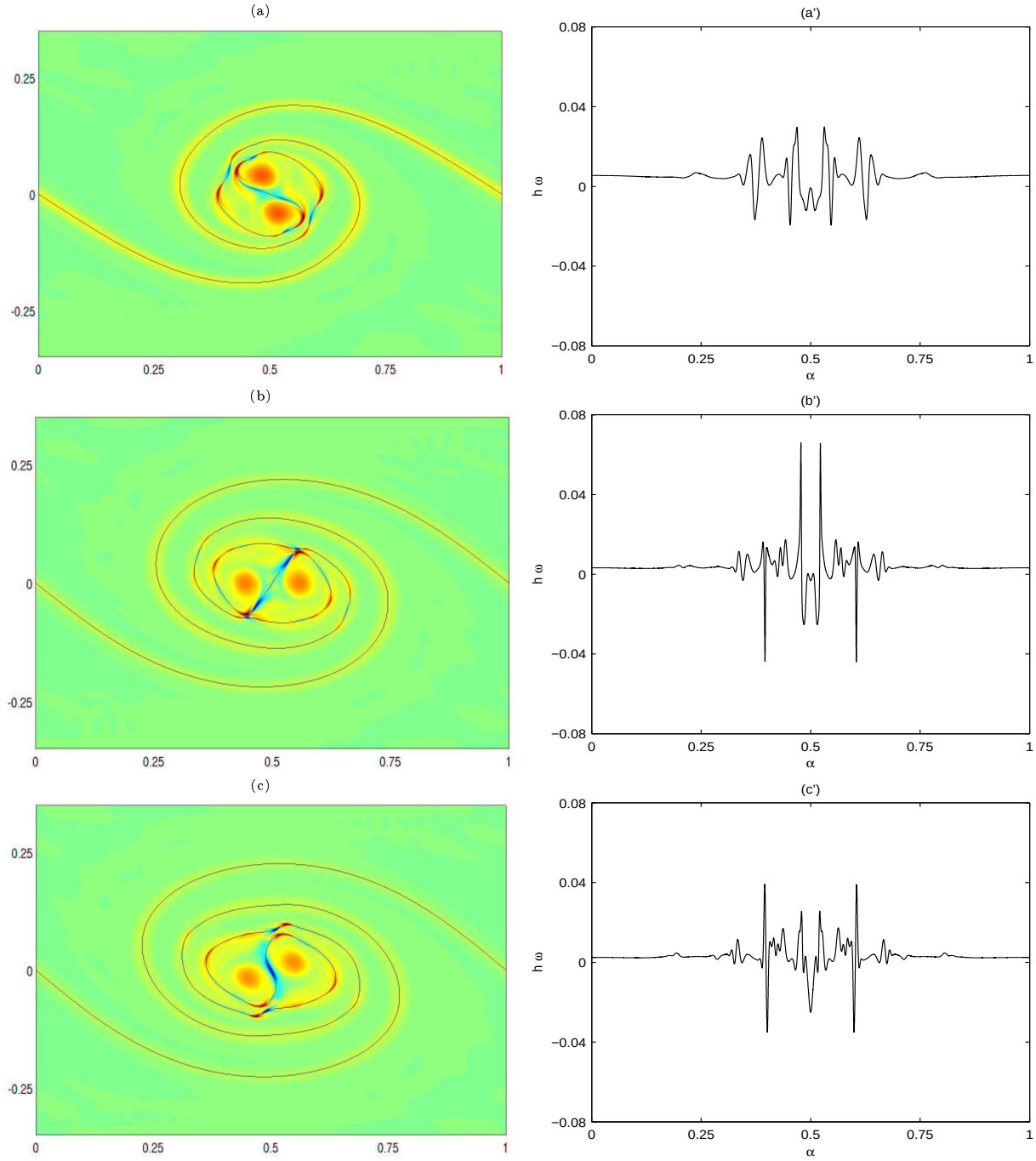

FIG. 22: Ceniceros and Roma, Physics of Fluids

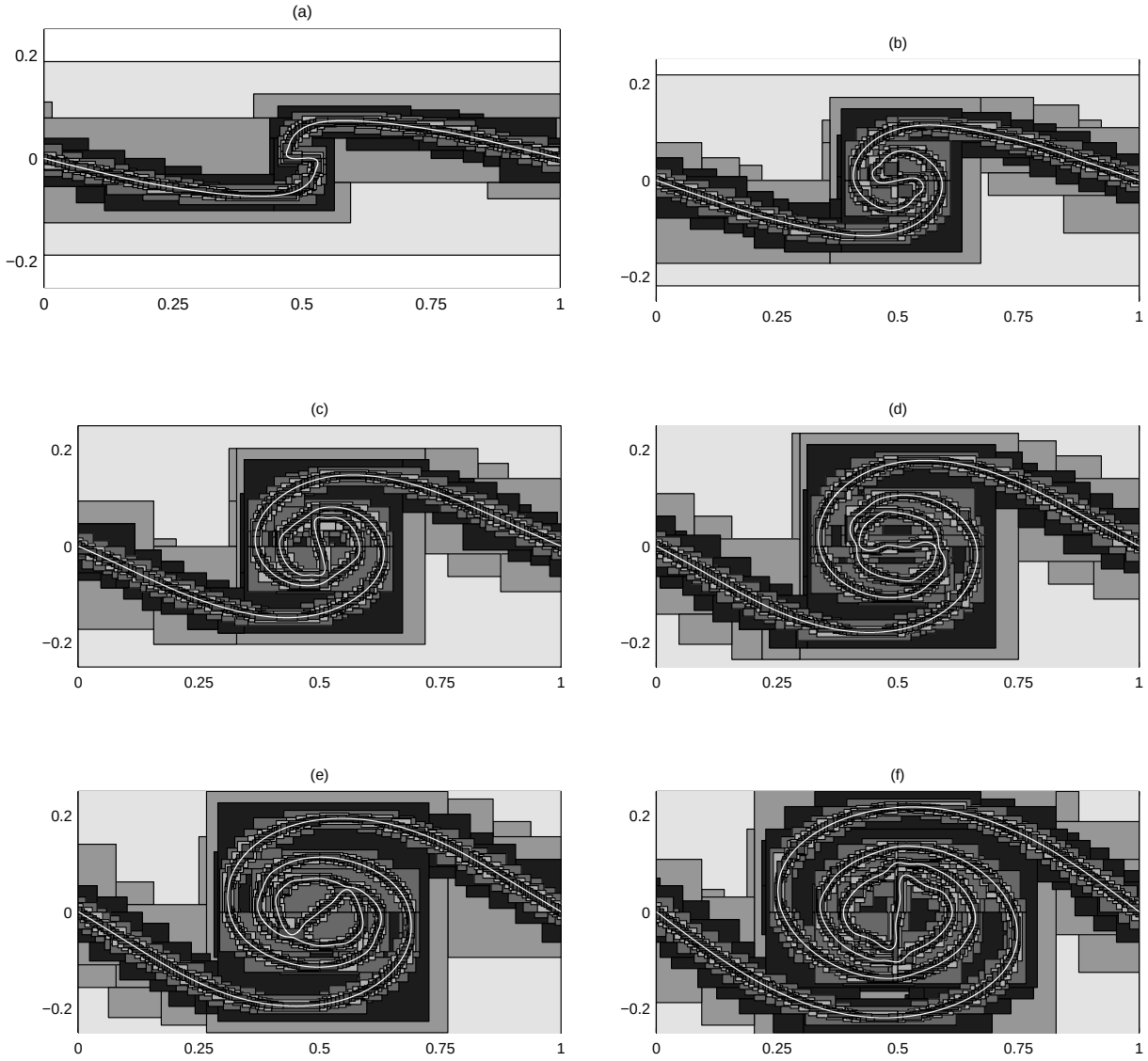

FIG. 23: Ceniceros and Roma, Physics of Fluids

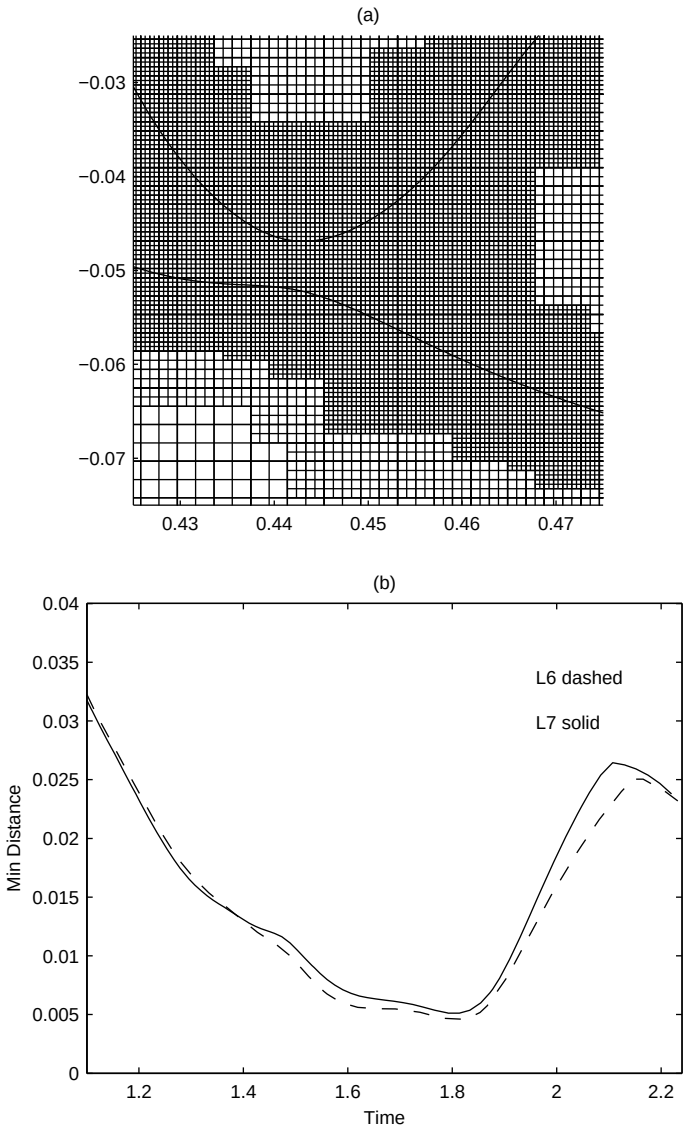

FIG. 24: Ceniceros and Roma, Physics of Fluids

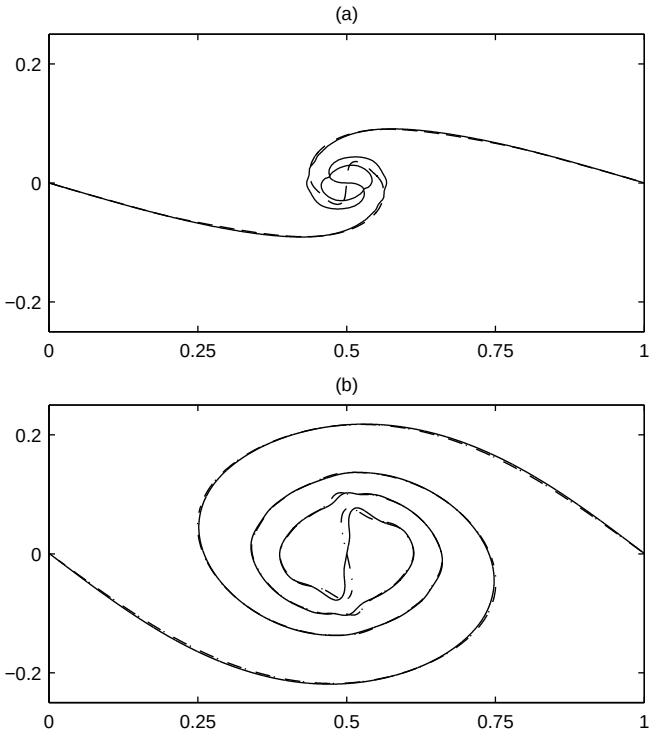

FIG. 25: Ceniceros and Roma, Physics of Fluids

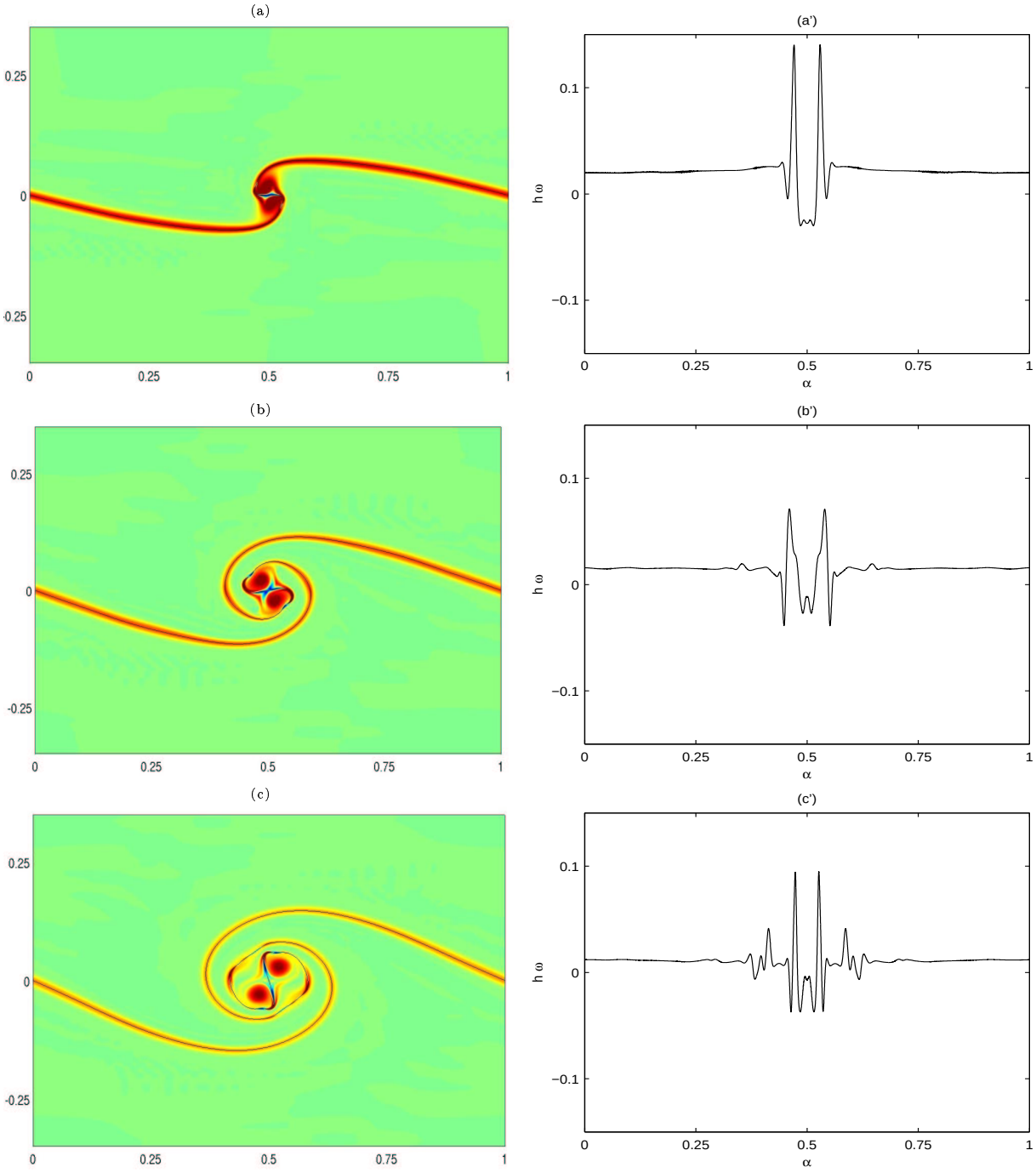

FIG. 26: Ceniceros and Roma, Physics of Fluids

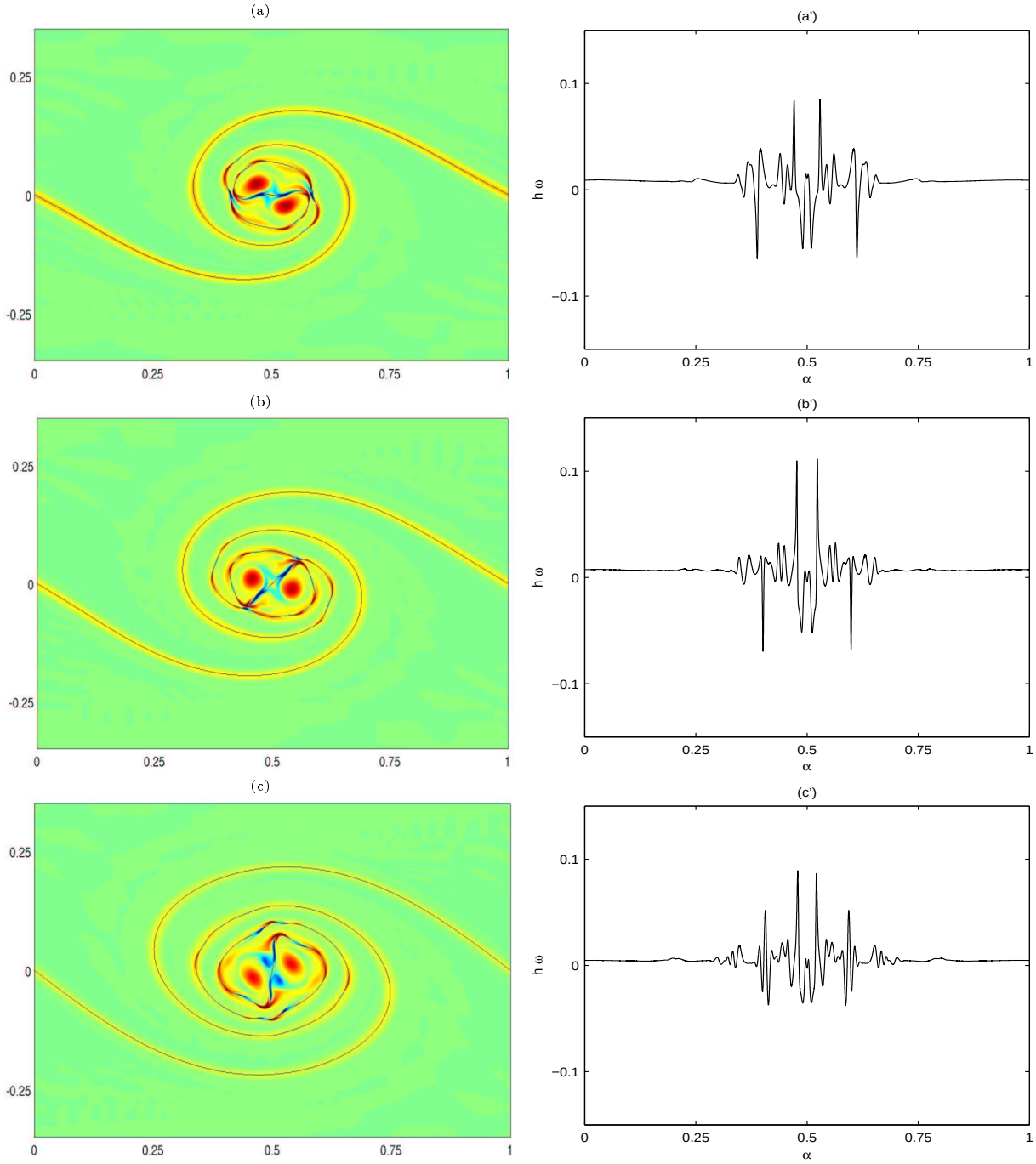

FIG. 27: Ceniceros and Roma, Physics of Fluids

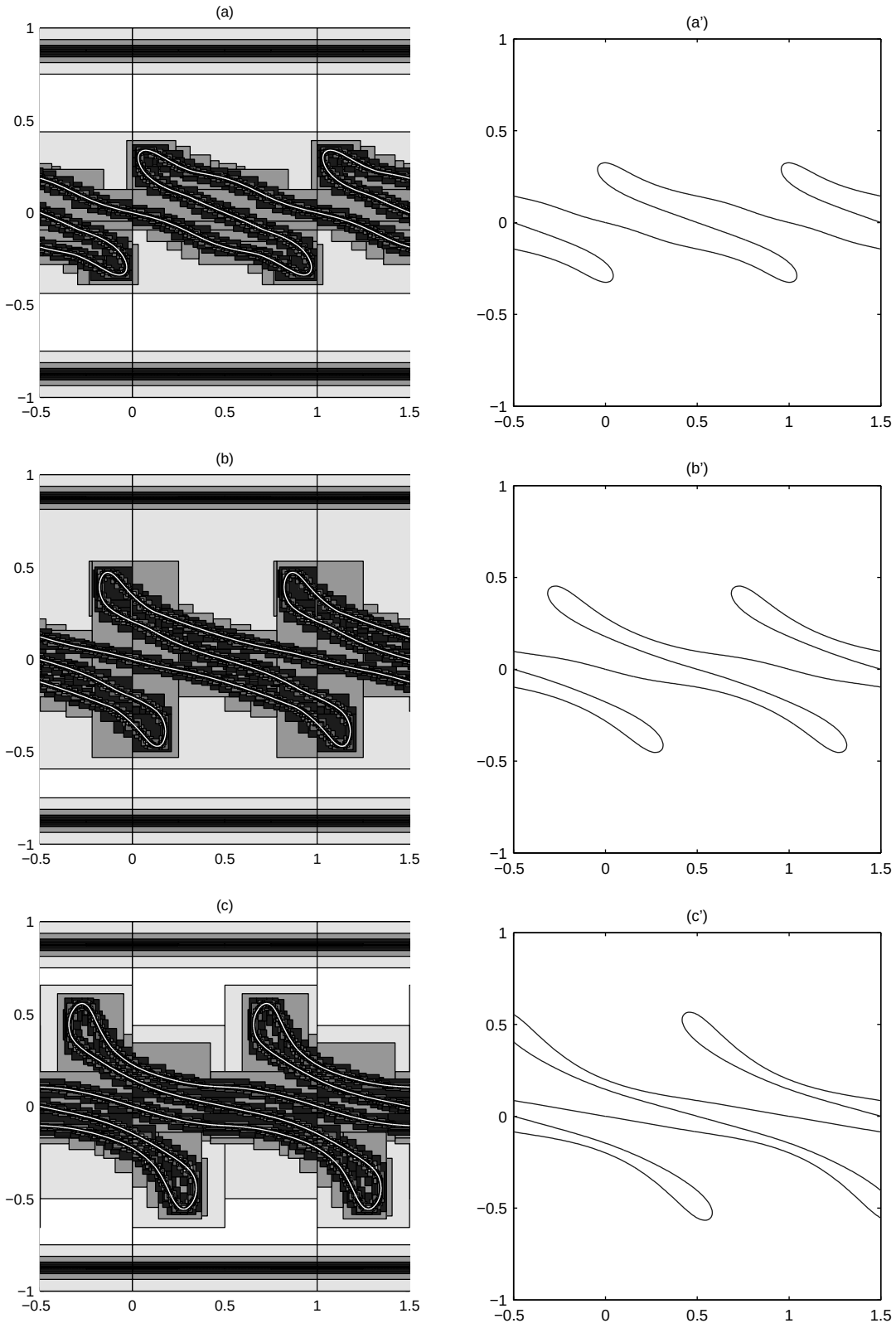

FIG. 28: Ceniceros and Roma, Physics of Fluids

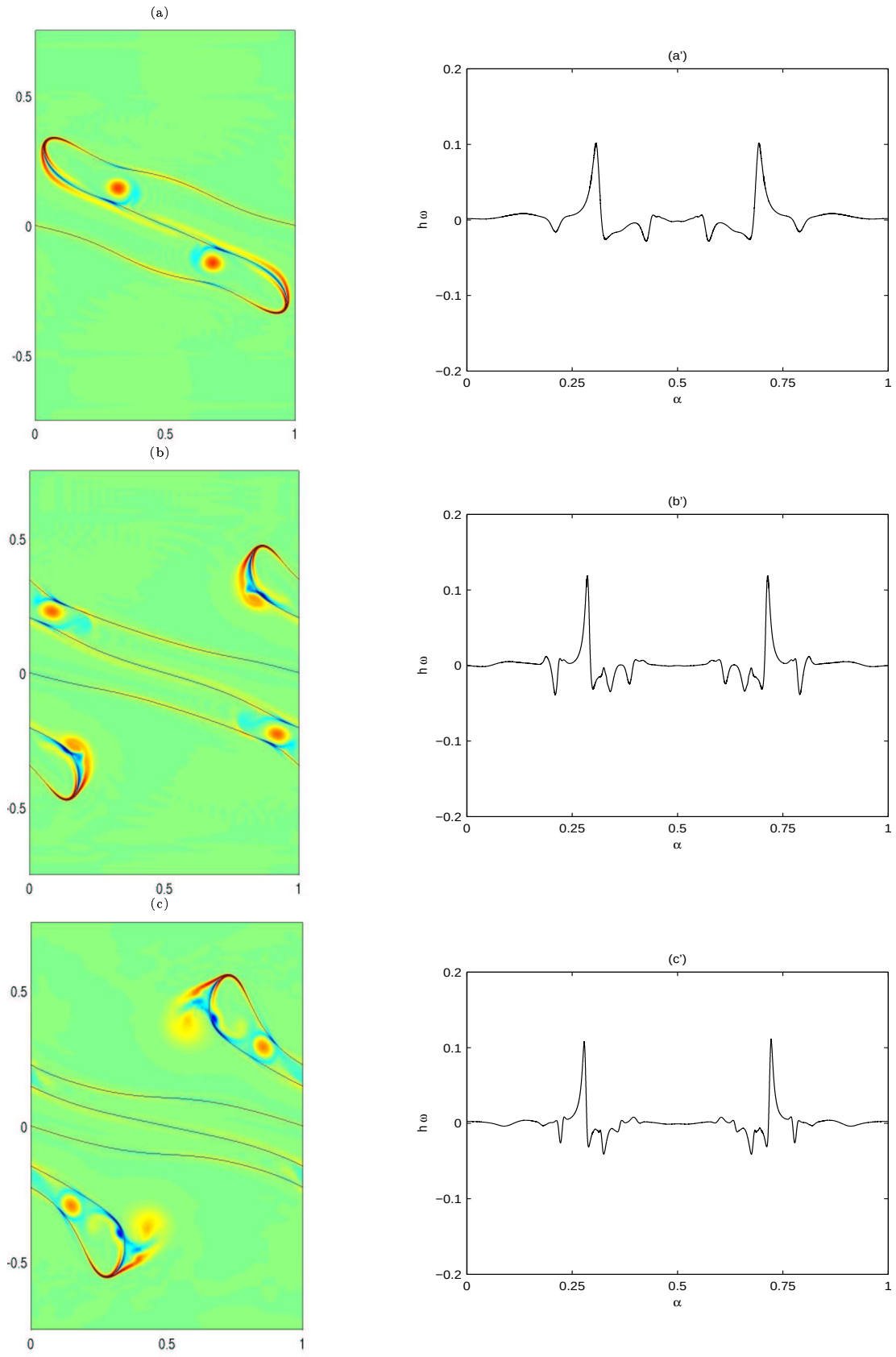

FIG. 29: Ceniceros and Roma, Physics of Fluids

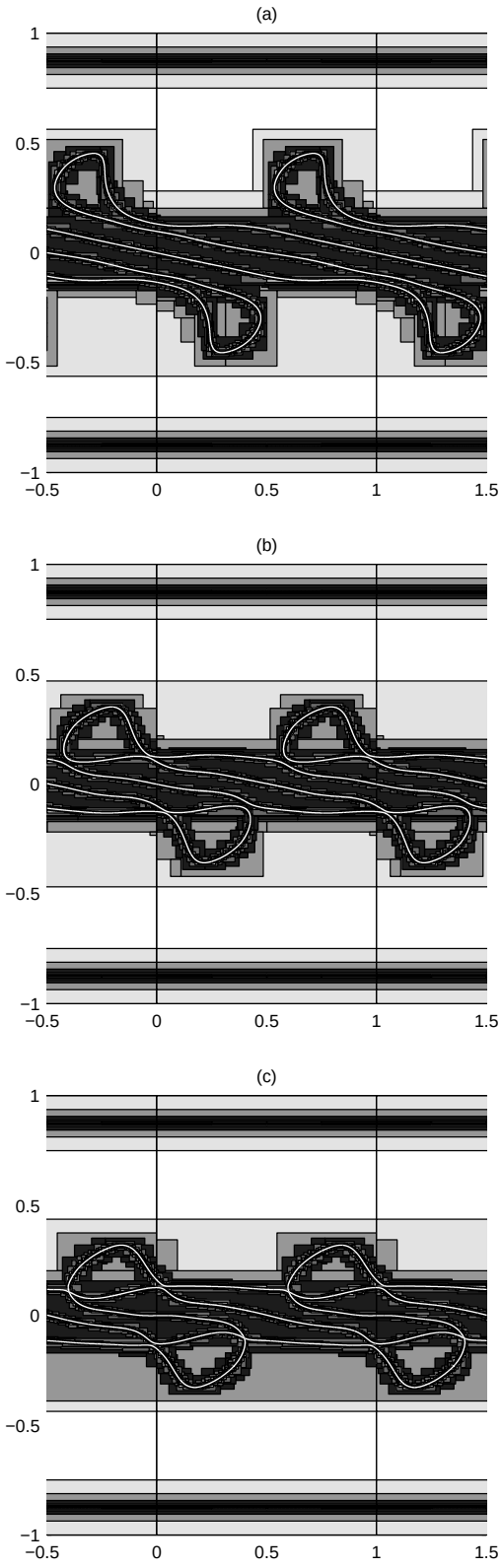

FIG. 30: Ceniceros and Roma, Physics of Fluids

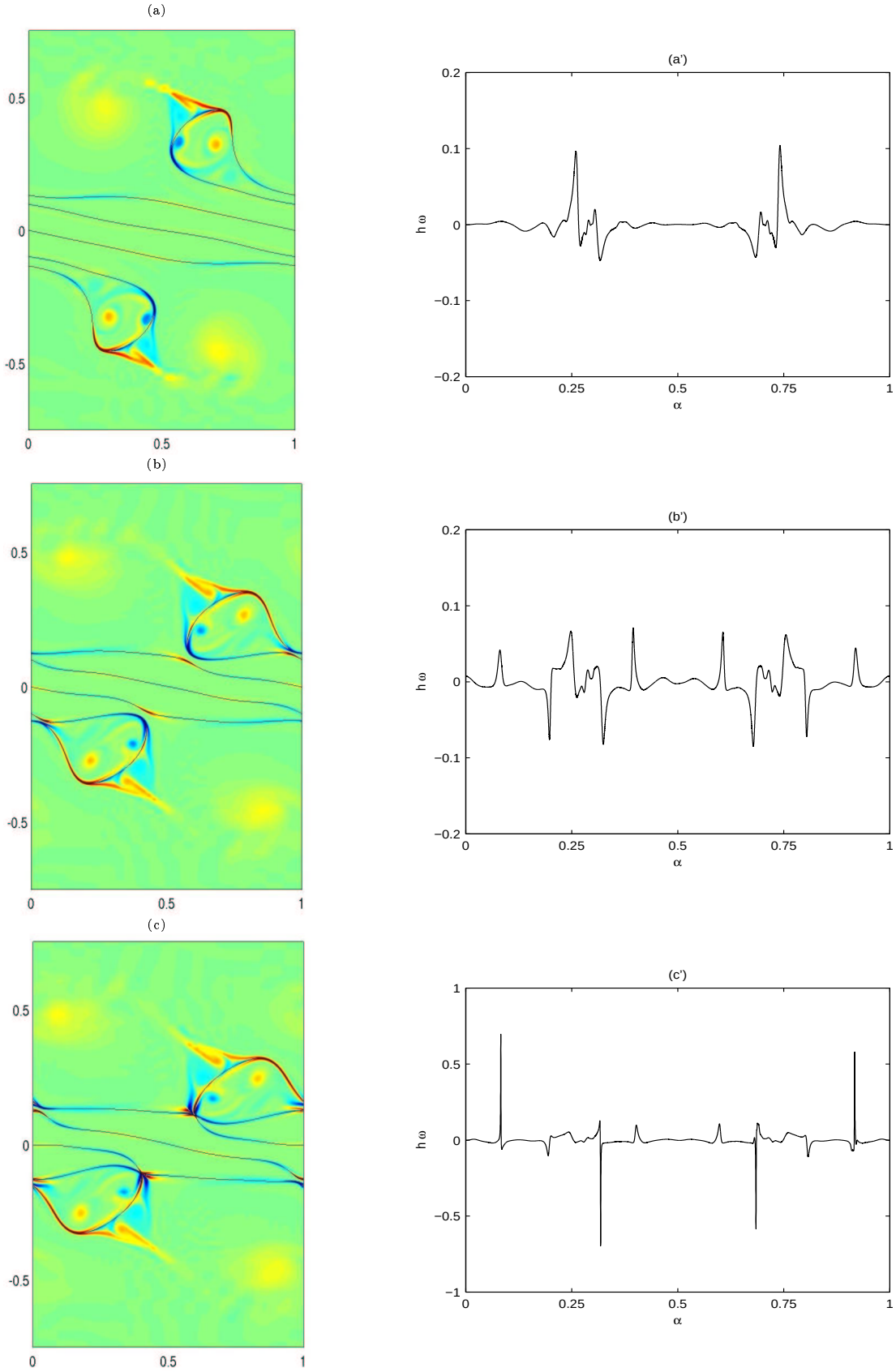

FIG. 31: Ceniceros and Roma, Physics of Fluids

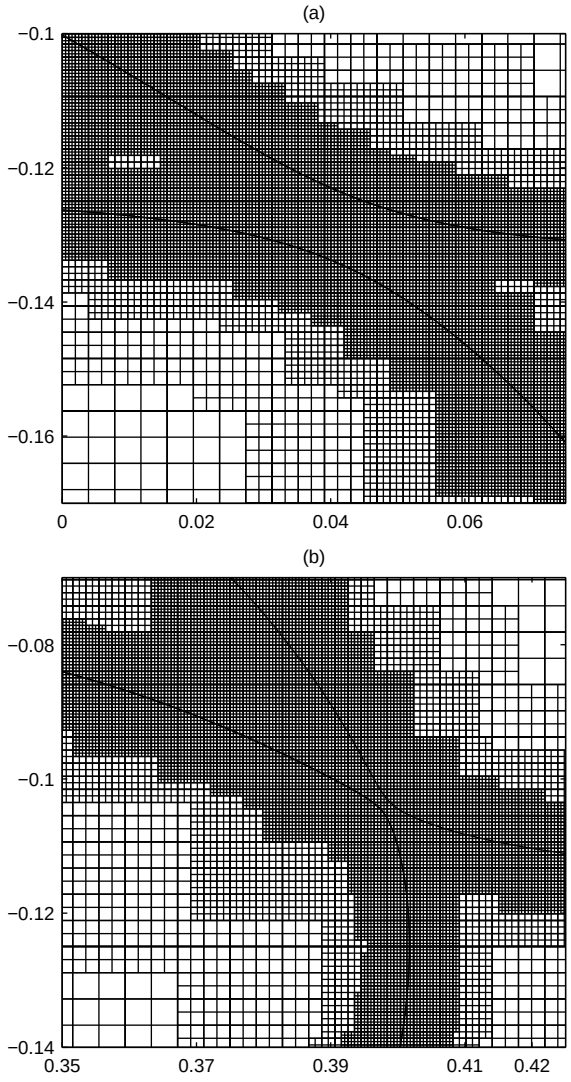

FIG. 32: Ceniceros and Roma, Physics of Fluids

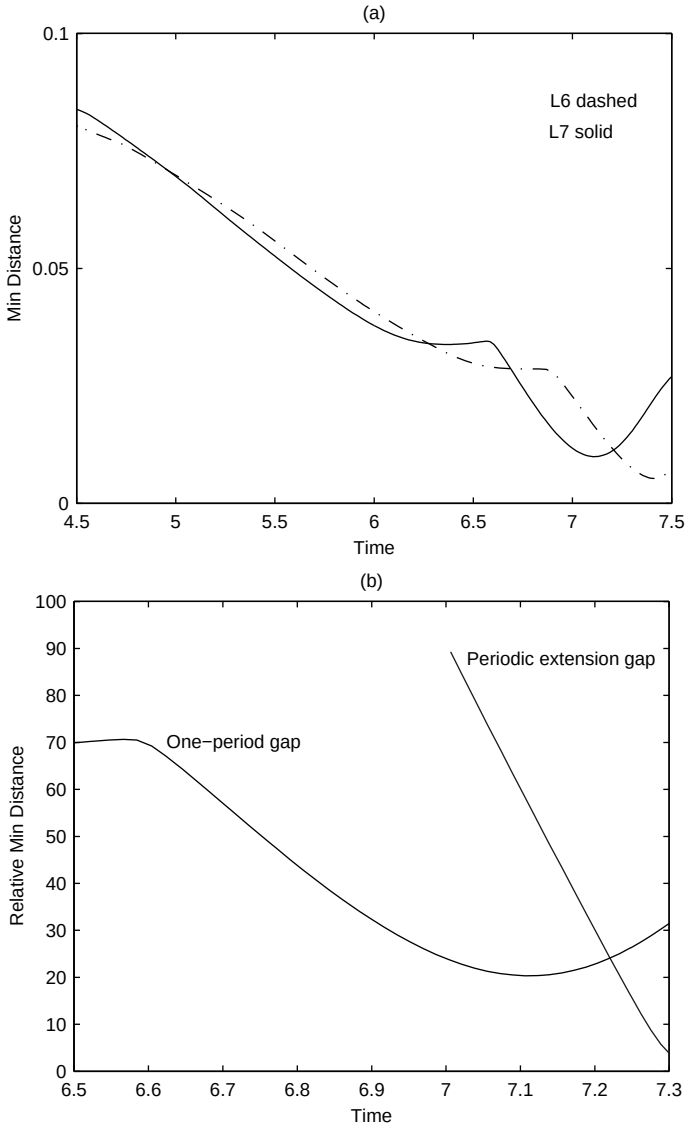

FIG. 33: Ceniceros and Roma, Physics of Fluids

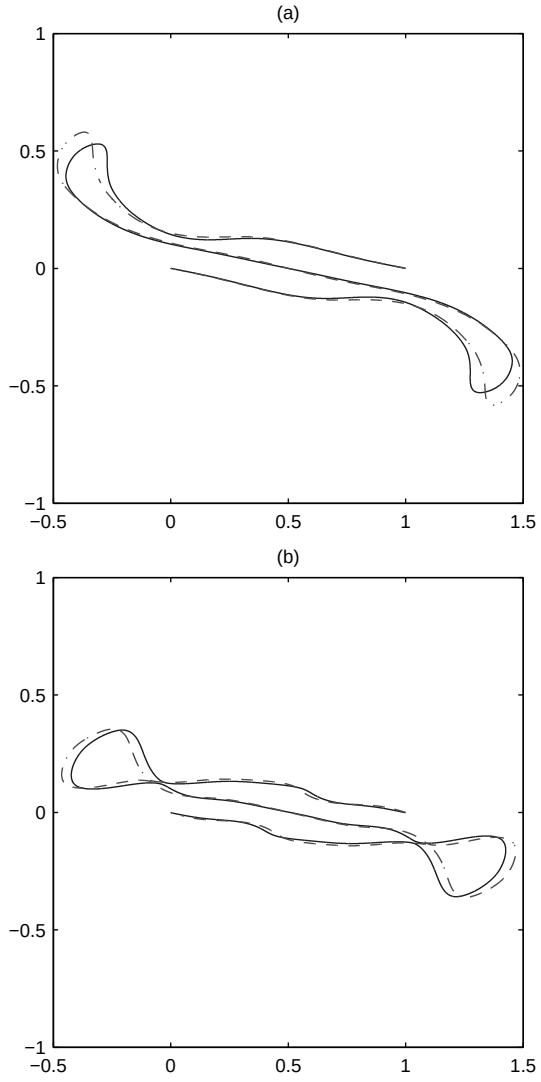

FIG. 34: Ceniceros and Roma, Physics of Fluids

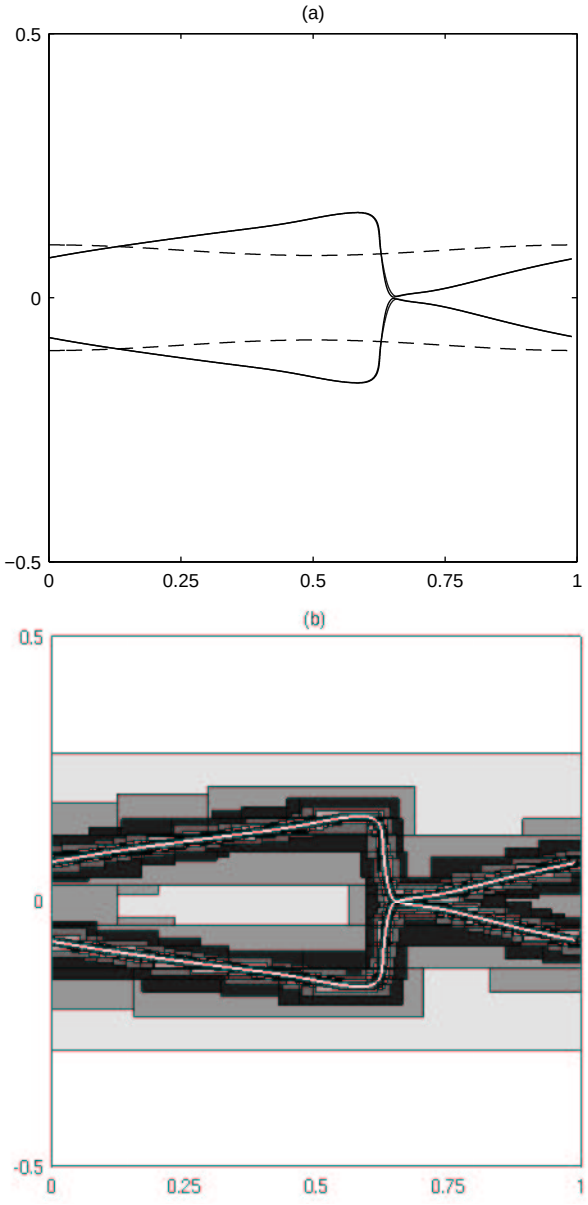

FIG. 35: Ceniceros and Roma, Physics of Fluids

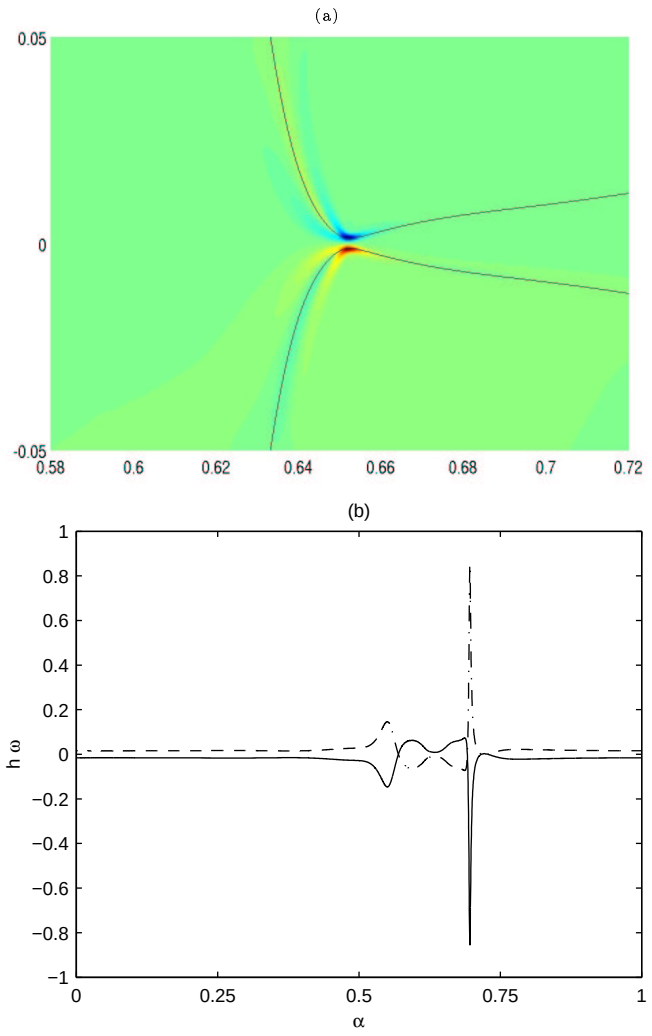

FIG. 36: Ceniceros and Roma, Physics of Fluids

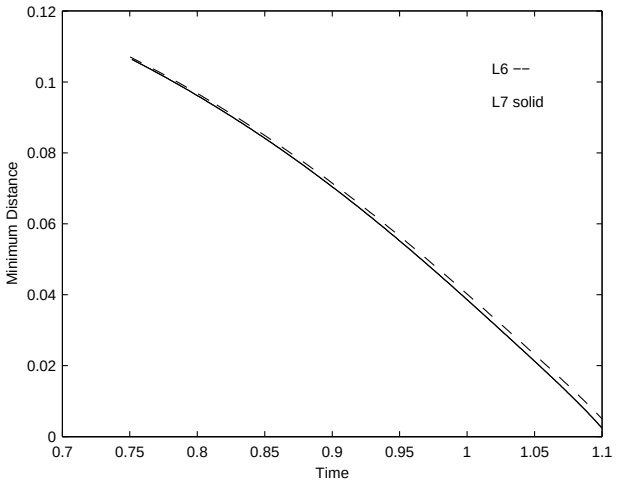

FIG. 37: Ceniceros and Roma, Physics of Fluids